Title

Receptive-field nonlinearities in primary auditory cortex: a comparative perspective.

Journal

Cerebral Cortex, 34(9)

Authors

Homma, Natsumi
See, Jermyn
Atencio, Craig
et al.

Publication Date

2024-09-03

DOI

10.1093/cercor/bhae364

Peer reviewed

OXFORD

Cerebral Cortex, 2024, **34**, bhae364
https://doi.org/10.1093/cercor/bhae364
Advance access publication date 12 September 2024
Original Article

Receptive-field nonlinearities in primary auditory cortex: a comparative perspective

Natsumi Y. Homma[1,2], Jermyn Z. See[1], Craig A. Atencio[1], Congcong Hu[1], Joshua D. Downer[1,3], Ralph E. Beitel[1], Steven W. Cheung[1], Mina Sadeghi Najafabadi[1], Timothy Olsen[1], James Bigelow[1], Andrea R. Hasenstaub[1], Brian J. Malone[1,3], Christoph E. Schreiner[1,*]

[1]John & Edward Coleman Memorial Laboratory, Kavli Institute for Fundamental Neuroscience, Department of Otolaryngology—Head and Neck Surgery, University of California San Francisco, San Francisco, CA, USA
[2]Department of Physiology, Development and Neuroscience, University of Cambridge, Downing Street, Cambridge, UK
[3]Center of Neuroscience, University of California Davis, Newton Ct, Davis, CA, USA

*Corresponding author: Christoph E. Schreiner, 675 Nelson Rising Lane, UCSF, San Francisco, CA, USA. Email: christoph.schreiner@ucsf.edu

Cortical processing of auditory information can be affected by interspecies differences as well as brain states. Here we compare multifeature spectro-temporal receptive fields (STRFs) and associated input/output functions or nonlinearities (NLs) of neurons in primary auditory cortex (AC) of four mammalian species. Single-unit recordings were performed in awake animals (female squirrel monkeys, female, and male mice) and anesthetized animals (female squirrel monkeys, rats, and cats). Neuronal responses were modeled as consisting of two STRFs and their associated NLs. The NLs for the STRF with the highest information content show a broad distribution between linear and quadratic forms. In awake animals, we find a higher percentage of quadratic-like NLs as opposed to more linear NLs in anesthetized animals. Moderate sex differences of the shape of NLs were observed between male and female unanesthetized mice. This indicates that the core AC possesses a rich variety of potential computations, particularly in awake animals, suggesting that multiple computational algorithms are at play to enable the auditory system's robust recognition of auditory events.

Key words: auditory cortex; receptive fields; nonlinearity; anesthesia; complex cells.

Introduction

Comparative studies employing congruent methods across groups can reveal similarities and differences in AC organization and function between species (Rauschecker 1997; Wang and Kadia 2001; Hoglen et al. 2018), brain structures (Hackett et al. 2001; Mackey et al. 2023), and brain states (Downer et al. 2015; Nourski et al. 2021). They allow the identification of conserved or diverging underlying neural properties and mechanisms. Furthermore, comparative studies between different sensory modalities, such as audition and vision, can provide broader insights into potentially common mechanisms in the processing of sensory information (Linden and Schreiner 2003; Nelken and Calford 2011; Rauschecker 2015). Here, we compare the cortical processing of complex sounds in A1 for several species and across awake and anesthetized animals while deploying virtually the same analytical approach. In particular, we examine the shape of the input/output functions ("nonlinearities" [NLs]) in primary auditory cortex (A1) spectro-temporal receptive fields (STRFs) by considering the role of three main influences: (i) the analysis method to derive STRFs, (ii) the animal species, and (iii) the overall brain state, by estimating the role of anesthesia on NLs and information processing.

STRFs are versatile models of the functional properties of cortical and subcortical auditory neurons (Aertsen and Johannesma 1981; Klein et al. 2000; Miller et al. 2001, 2002; Atencio and Schreiner 2013). STRF models are usually instantiated as a single or a set of linear filters followed by nonlinear gain functions, or NLs, that translate the match of a stimulus to the filters into a firing rate (Lian et al. 2021; Atencio and Schreiner 2013; Sharpee 2013, 2014), providing a linear-nonlinear model of neuronal processing (Chichilnisky 2001; Dayan and Abbott 2001; Sharpee 2016; Meyer et al. 2017). The integrative filters capture *what* stimulus properties are relevant for the neuron's role. By contrast, the NLs characterize *how* this stimulus information is converted into the neuron's output signal. Combined, filter shape and NL gain attributes provide a basis for understanding neuronal processing. NL shape can be reasonably approximated as a combination of a linear and a quadratic term (Marmarelis and Marmarelis 1978; Marmarelis 1997; Victor and Purpura 1998). Two general types of NLs can be distinguished: when the linear term dominates the NL shape, the resulting NL is asymmetric (see Fig. 1 top row); if the quadratic term dominates the NL results in a more symmetric shape (see Fig. 1 bottom row; Fitzgerald et al. 2011; Rajan and Bialek 2013; Sharpee 2013; Shih et al. 2020).

Many cortical and subcortical sensory neurons are well approximated by asymmetric NL functions, including those of the dominant filter of subcortical and cortical cells in the auditory system (Atencio and Schreiner 2012; Shih et al. 2020) and "simple cells" in visual cortex (Lian et al. 2021). By contrast, linear-nonlinear models with symmetric NLs have been found to account for various other neuronal response types, including those of "complex cells" in visual cortex (Movshon et al. 1978; De Valois et al. 1982; Pollen and Ronner 1982; Skottun et al. 1991; Freeman et al. 2013), multidigit neurons in somatosensory cortex (Pramodsingh

Received: July 6, 2023. **Revised:** August 14, 2024. **Accepted:** August 21, 2024

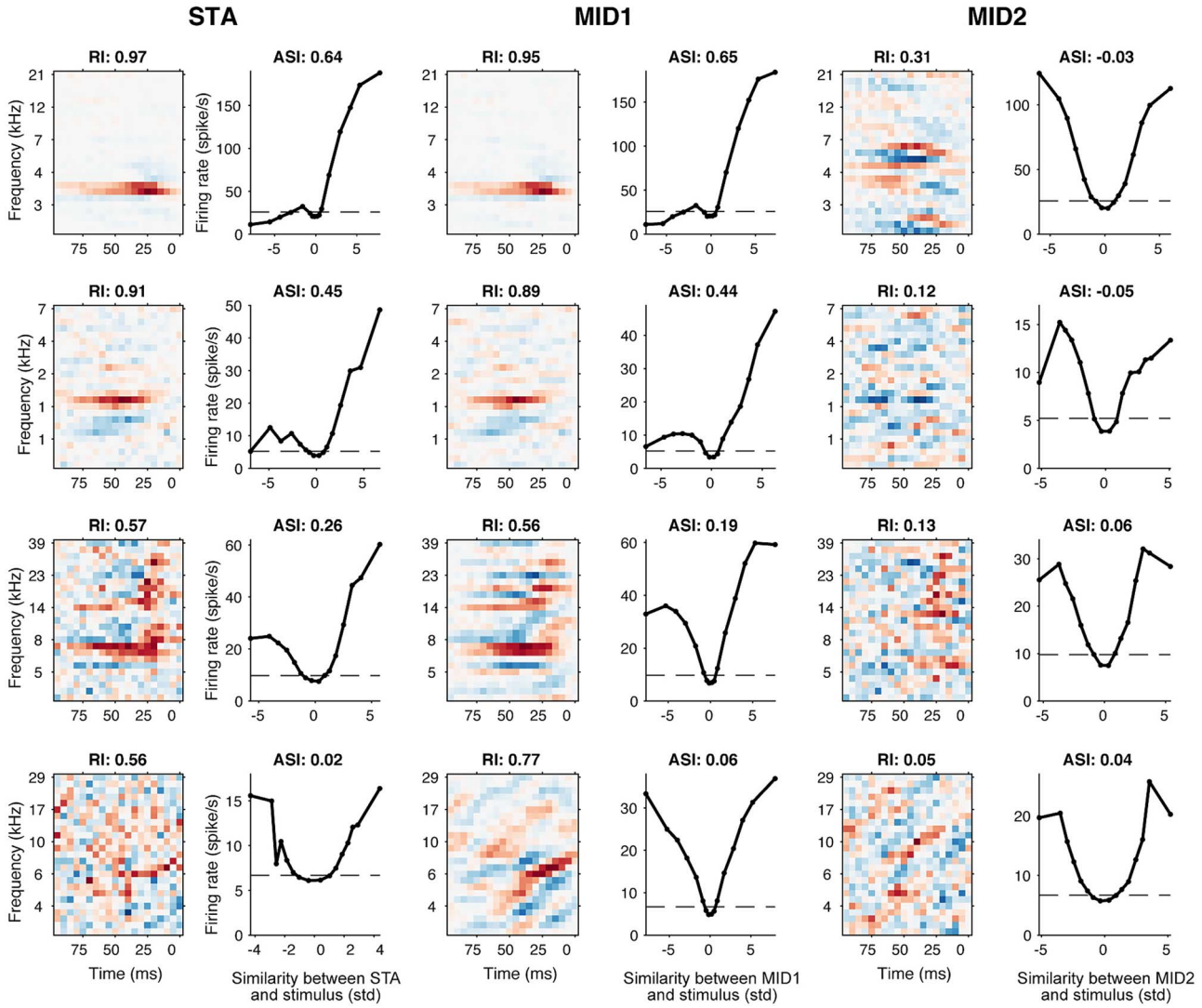

Fig. 1. Receptive fields and their nonlinearities of four neurons from core auditory cortex of alert squirrel monkeys. 1st column: STRFs from STAs. Frequency versus time before spike occurrence. RI: Reliability index. 2nd column: STA nonlinearity; firing rate versus projection values, i.e. correlation between stimulus and STRF (std: Standard deviations). The dashed line represents the average firing rate over the complete stimulus presentation, which is closer to the minimum firing rate reflecting nonspecific spiking for lower similarity between STRF and stimulus. On the other hand, spikes driven at higher similarity between STRF and stimulus are specific to stimulus envelope or properties supporting a higher firing probability. ASI: Asymmetry index. 3rd column: STRFs from primary maximally informative dimension (MID1s). 4th column: MID1 nonlinearities. 5th column: STRFs from secondary maximally informative dimension (MID2s). 6th column: MID2 nonlinearities.

et al. 2012), and are also associated with secondary filters in A1 neurons (Atencio et al. 2008, 2009). Studies in A1 of anesthetized cats and rats, however, have identified only a small number of neurons where the dominant filter is also associated with a more symmetric NL (Atencio et al. 2008; Atencio and Schreiner 2012; Sharpee 2013; Homma et al. 2021).

Neurons in visual cortex are commonly classified as simple or complex based, partially, upon their sensitivity to the sign of stimulus contrast (e.g. Rust et al. 2005). Simple cells can be modeled with asymmetric NLs and described as local feature detectors with intolerance to contrast phase and stimulus transformations like changes in position (Movshon et al. 1978; De Valois et al. 1982; Pollen and Ronner 1982; Skottun et al. 1991). By contrast, complex cells are insensitive to the sign of the stimulus contrast that can be modeled through a symmetric nonlinearity (Movshon et al. 1978; De Valois et al. 1982; Pollen and Ronner 1982; Skottun et al. 1991). It should be noted that a full characterization of complex cells requires a more elaborate model, e.g. two linear filters in quadrature phase (Kouh and Poggio 2008; Sharpee 2016; Lian et al. 2021). In auditory cortex, however, computational and behavioral advantages of neurons with similar distinctions as in the visual cortex, including symmetric versus asymmetric NLs, remain largely unknown.

Species-specific differences in the cellular and structural organization of cortex may play an important role in shaping NLs. In visual cortex, the relative proportion of complex cells has been shown to vary between cortical layers and across species (Van Hooser 2007; Van den Bergh et al. 2010; Niell and Stryker, 2008; Ziemba et al. 2019). This suggests that their expression might be governed by diversity in cortical spatial organization, synaptic connectivity, and intrinsic cellular properties of neurons across cortical fields, as well as between species. Additionally, the apparent functional characteristics of neurons appear to be influenced by the brain state in which they were derived, and can manifest differently in anesthetized, passively awake, or in actively behaving animals (Fritz et al. 2005; Ahrens

et al. 2008; Christianson et al. 2008; David 2018; Elgueda et al. 2019).

Finally, the methods used to ascertain STRF models can also affect their characterization. Linear receptive field estimation approaches, such as the commonly used spike-triggered averaging (STA), may not allow identification of certain NL types (Sharpee 2013) and are also affected by stimulus statistics and context (Suga et al. 1983; Kvale and Schreiner 2004; Sadagopan and Wang 2009; Williamson et al. 2016; David 2018). Some of these shortcomings can be alleviated by using dimensionality reduction techniques, such as most informative dimensions (MIDs), to derive more completely the components of linear-nonlinear models (Sharpee et al. 2004; Rajan and Bialek 2013; Sharpee 2013; Atencio and Schreiner 2013; Atencio and Sharpee 2017).

In this comparative analysis, we found a larger proportion of symmetric NLs in awake squirrel monkey and mouse A1 than in anesthetized monkeys, cats, and rats revealing a dependence of the configuration of gain NLs on brain states.

Methods

Animal preparation

All procedures related to the maintenance and use of animals in this study were approved by the Institutional Animal Care and Use Committee of the University of California–San Francisco and followed guidelines of the National Institutes of Health for the care and use of laboratory animals. Due to housing and breeding constraints for the larger species, we used female animals except for mice, in which we utilized three male and two female animals.

Awake Squirrel monkey: The methodological details for these experiments have been described previously (Malone et al. 2013, 2017), but are briefly repeated here. Seven adult female squirrel monkeys (*Saimiri sciureus*; SqM) were trained to sit quietly in a restraint chair. Animals were then implanted with headposts to allow for head fixation during physiological recordings. During all surgical procedures, anesthesia was induced with ketamine (25 mg/kg, i.m.) and midazolam (0.1 mg/kg) and the animals were maintained in a steady plane of anesthesia using isoflurane gas (0.5–5%). Implants were secured to the skull using bone screws and dental acrylic. After animals were trained to sit in the primate chair with their head fixed to a frame, they underwent a second surgery to implant a recording chamber over the AC. The temporal muscle was partially resected, the cranium overlying AC was exposed, and a 10-mm-diameter chamber was secured using bone screws and dental acrylic. Perioperative pain management included local application of bupivacaine, as well as buprenorphine (0.01–0.03 mg/kg) and meloxicam (0.3 mg/kg) as needed. Sterile procedures were used to expose and record from AC. A 2–3 mm hole was opened within the chamber using a sterile hand drill. Animals were allowed to recover after surgery for at least 1 week before recordings were performed. After each recording session, the chamber was filled with antibiotic ointment and sealed with a metal cap. Recordings took place up to 3 times a week over a period of up to 6 months.

Awake Mouse: A total of five adult mice (three male and two female) served as subjects. All mice had a C57BL/6 background and expressed optogenetic effectors targeting interneuron subpopulations, which were not manipulated in the current study (Bigelow et al. 2019; Olsen and Hasenstaub 2022). Surgical procedures were performed under isoflurane anesthesia with perioperative analgesics (lidocaine, meloxicam, and buprenorphine) and monitoring. A custom stainless steel headbar was affixed to the cranium above the right temporal lobe with dental cement, after which subjects were allowed to recover for at least 2 days. Prior to electrophysiological recording, a small craniotomy (~1–2 mm diameter) centered above AC (~2.5–3.5 mm posterior to bregma and under the squamosal ridge) was made. The craniotomy was then sealed with silicone elastomer (Kwik-Cast, World Precision Instr.). The animal was observed until ambulatory (~5–10 min) and allowed to recover for a minimum of 2 h prior to electrophysiological recording. The craniotomy was again sealed with silicone elastomer after recording, and the animal was housed alone thereafter. Electrophysiological recordings were conducted up to 5 consecutive days following the initial craniotomy.

Anesthetized Squirrel monkey: Recordings were made in four adult female squirrel monkeys (*S. sciureus*). For the craniotomy, anesthesia was induced with ketamine (25 mg/kg, i.m.) and midazolam (0.1 mg/kg) and the animals were maintained in a steady plane of anesthesia using pentobarbital sodium (Nembutal; 15–30 mg/kg) or isoflurane gas (0.5–5%). Surgery consisted of a tracheotomy, reflection of the soft tissues of the scalp, craniotomy over AC and durotomy. At the completion of a craniotomy (~5×5 mm over the AC) under isoflurane, the anesthetic agent was switched to ketamine/diazepam (2–5 mg·kg h ketamine/0.2–0.5 mg·kg·h diazepam) to effect and maintained during the terminal recording session.

Anesthetized Cats: Five adult female cats were sedated with an initial dose of ketamine (22 mg/kg) and acepromazine (0.11 mg/kg) and then anesthetized with pentobarbital sodium (Nembutal; 15–30 mg/kg) for the surgical procedure (Atencio et al. 2008, 2009; Shih et al. 2020). Bupivacaine was applied to incisions and pressure points. Surgery consisted of a tracheotomy, reflection of the soft tissues of the scalp, craniotomy over AC (~6×6 mm) and durotomy. During the recording period pentobarbital was discontinued and, to maintain an areflexic state, the animal received a continuous infusion of ketamine/diazepam (2–5 mg·kg·h ketamine/0.2–0.5 mg·kg h diazepam in lactated ringer solution).

Anesthetized Rats: Twenty-six female Sprague–Dawley rats (wild-type) sourced from Charles River were used in this study. The surgical procedures were described in detail previously (Homma et al. 2020, 2021). Anesthesia was induced with ketamine hydrochloride (100 mg/kg) and xylazine hydrochloride (3.33 mg/kg) and maintained with a mixture of ketamine (10–50 mg/kg) and xylazine (0–20 mg/kg). Atropine sulphate, dexamethasone sodium phosphate and meloxicam were administered for therapeutic purposes. Local lidocaine hydrochloride was used prior to incisions. Following a tracheotomy, the skin and muscle over one hemisphere of the AC was removed, a craniotomy window (~3×5 mm) was made, and the dura was removed. Silicone oil was used to cover the cortex.

Stimulus synthesis

All sound stimulus generation and data analysis were performed using MATLAB (R2019a, Mathworks) with the Statistics and Machine Learning toolbox (Version 11.5). We synthesized a dynamic moving ripple (DMR) that contained 50 sinusoidal carrier frequencies per octave (0.5–40 kHz) with random phases (Escabi and Schreiner 2002; Atencio et al. 2008). The spectro-temporal envelopes were generated with a maximum of 4 cyc/oct spectral modulation frequencies (SMFs), a maximum of 40 Hz (rats, cats, mice) or 150 Hz (monkey) temporal modulation frequencies (TMFs), and a maximum 40 dB spectro-temporal modulation depth. We set the mean intensity to 60–70 dB SPL.

Electrophysiological recordings

All recordings were made in soundproof chambers (Industrial Acoustics). Auditory stimulus presentation and neural data acquisition were computer controlled using either RHD2000 Interface software (Intan Technologies), a Neuralynx Cheetah System, or a TDT RX-5 amplifier and Brainware software (Tucker-Davis Technologies). Sound stimuli at a 96 kHz (192 kHz for mice) sampling rate were presented either contralaterally using a closed electrostatic speaker (EC1, Tucker-Davis Technologies; rat; or SRX MK3, Stax, Japan; cat), or with a dynamic insert earphone (ER1, Etymotic Research; anesthetized SqM). Free-field stimuli were delivered via an electrostatic speaker (ES1, Tucker-Davis Technologies) positioned 15–20 cm from the contralateral ear (mice) or using a free-field speaker (Sony SS-MB150H) 40 cm in front of the animal (awake SqM).

Target locations were selected based on pure tone mapping (tungsten electrodes) of the tonotopic gradient of A1 in the anesthetized experiments. We pseudo-randomly presented 675 different pure tones (50 ms, 0.5–32 kHz in 0.13 octave steps, 0–70 dB SPL in 5 dB increments) to determine the frequency response area (FRA). Once a target location was identified, we inserted a multicontact silicon probe array (Neuronexus or Cambridge NeuroTech) perpendicularly to the pial surface to a depth of ∼0.9 to ∼1.65 mm (dependent on the species). We presented the DMR for 10–30 min (awake monkey: 10 or 30 min; awake mouse: 10 min; anesthetized monkey: 20 min; cats and rats: 15 or 20 min). The probes had 16 (cat), 32 or 64 (rat, mouse, squirrel monkey) recording channels vertically arranged with 150, 50, or 20 μm dorso-ventral spacing, respectively. Neural traces were band-pass filtered between 0.6 and 6 kHz and digitized at 17.8–27.1 kHz sampling rate. Single units were identified offline using either MountainSort (Chung et al. 2017), Kilosort2 (https://github.com/MouseLand/pykilosort/tree/master/ pykilosort), or a Bayesian spike-sorting algorithm (Lewicki 1994; Atencio and Schreiner 2013).

Estimation of spectro-temporal receptive field

For analysis, we down-sampled the DMR stimulus to a resolution of 0.1 octave and 5 ms. The envelope amplitude was dB scaled. We used a reverse correlation method, STA, to obtain STRFs by averaging 100 ms of spectro-temporal stimulus envelope immediately preceding a spike (Escabi and Schreiner 2002; Atencio and Schreiner 2012, 2013). We also applied most informative dimension (MID) analysis to obtain multidimensional STRFs (Sharpee et al. 2004, 2006; Atencio et al. 2008, 2009; Homma et al. 2021). We divided the data into four segments for a jackknife estimate. For each estimate, a different 3/4 of the data was used as training data set. The remaining 1/4 of the data was used as test data set. The first MID (MID1) was estimated with iterations to maximize mutual information (MI) between stimulus and spike train. The second MID (MID2) was estimated by searching the stimulus space for another receptive field component that further increased the information. The iterations for MID2 were terminated when the information on the test set using the estimated MID2 achieved a maximum and before the information from the test set decreased while the information from the training set continued to increase. This early-stopping procedure limited over-fitting.

To calculate the MI between stimulus and spikes, each stimulus segment s that evoked a spike was projected onto a filter V using the inner product $z = s \bullet V$, where V was the STA, MID1 or MID2. The projection values (z) were then binned to compute the probability distribution $P_V(z|spike)$. To have a clearer visualization, we set the bin edges based on the percentiles of the projection values (0, 0.25, 0.5, 1, 2, 5, 10, 20, 50, 80, 90, 95, 98, 99, 99.5, 99.75, 100). Positive projection values indicate that high-energy portions of the stimulus fall on excitatory parts of the filter and low-energy portions on inhibitory parts of the filter. Negative values mean that stimulus and filter are anticorrelated. The prior stimulus distribution, $P_V(z)$, was estimated by projecting all stimuli onto the filter V regardless of a spike occurrence. To normalize the projection values, the units of $P_V(z|spike)$ and $P_V(z)$ were transformed to standard deviation using $x = (z—\mu)/\sigma$, where μ and σ were the mean and standard deviation of all the prior projection values.

The nonlinearity (NL) is a characterization of the input–output function for each filter and was estimated as $P_V(spike|x) = P_V(spike) * (P_V(x|spike)/P_V(spike))$, where $P_V(spike)$ is the average firing rate of the neuron (Agüera et al. 2003; Atencio et al. 2008; Shih et al. 2020). The shape of each NL was characterized by an asymmetry index (ASI). The ASI is defined as $(R-L)/(R+L)$ where R and L are the sums of NL values that correspond to projection values > 0 or < 0, respectively. ASI values near 0 indicate a symmetric NL, implying that the neuron responds independent of the stimulus phase or polarity. ASIs near +1 or −1 indicate neurons that have an increased probability of spiking when the stimulus is either positively or negatively correlated with the filter, respectively.

The MI for a filter V and single spikes was estimated using the following function: $I(V) = \int dx P_V(x|spike) \log_2 [P_V(x|spike)/P_V(x)]$. For the information calculation, we used a conventional binning method, and the normalized projection values (x) were binned for the range of −7 to 7 by one increment. Although we observed a slight increased estimation for the information compared to the percentile binning, the selection of binning methods had only minor differences. The joint MI for the two MIDs was determined as

$I(MID1, MID2) = \int\int dx1,dx2\, P_{MID1,MID2}(x1,x2|spike) \log_2 [P_{MID1,MID2}(x1,x2|spike)/P_{MID1,MID2}(x1,x2)]$; x1 and x2 represent the projection values of the stimulus onto the first and second dimensions, MID1 and MID2, respectively. $P_{MID1,MID2}(x1,x2)$ presents the prior probability distribution of dimension MID1 and MID2, and $P_{MID1,MID2}(x1,x2|spike)$ is the probability distribution calculated only from the stimulus segments that evoked a spike. To account for the size of a data set, the information value for unlimited data set size was estimated using an extrapolation procedure (Efron and Tibshirani 1994; Atencio et al. 2008). We calculated information values over 90–100% of test data set (1/4 of the data set) in 2.5% increments for each segment. The information calculated for the fractioned data was plotted against the inverse of the data fraction percentage (1/90, 1/92.5, 1/95, 1/97.5, 1/100), a linear fit was made, and the y-intercept was the estimated information value for the test set.

A reliability index (RI) metric was used to quantify the strength of STRFs. RI was estimated as the mean value of stimulus/filter correlation coefficient for the combinations of STRFs obtained from the four segments of the jackknife procedure. This was a comparable method to calculating RI of STAs by segmenting a spike train and estimating STRF similarity with iterations (Escabi et al. 2014; See et al. 2021).

STRF best frequency (BF) and spectral bandwidth (BW) were estimated using the combined excitatory and inhibitory portions after converting the magnitude of each STRF bin to absolute values and constructing the marginal frequency distribution. BF refers to the mode of the (rectified) STRF marginal of each filter after summation along the time axis (Homma et al. 2021). BW was computed as the width of the summed function that exceeded 70% of its maximum value. This criterion was selected to focus on the main frequency response region and to avoid potentially

spurious side peaks. Sharpness of tuning was defined here as Q = BF/BW.

Statistical analysis

Non-parametric methods were used for all statistical analysis, and the results are summarized in the Supplemental Table 1. For comparing different species and anesthesia effects, Kolmogorov–Smirnov tests were used followed by Dunn's test for post hoc comparison. For comparing properties between filters (STA, MID1, and MID2), nonparametric paired t-test (Wilcoxon signed rank test) was used. For examining the effect of recording duration on ASIs and firing rates, Friedman test, a nonparametric one-way ANOVA with repeated measures, was used followed by Dunn's test for post hoc comparisons. For correlation analysis, Spearman's rho (r_s) value was computed.

The significance of NLs was estimated by using a resampling procedure. Each NL was re-estimated by randomly sampling, without replacement, 95% of the projection values related to a spike (posterior projection value distribution). Then the NL was re-estimated. This procedure was completed 100 times. To define the NL significance, we circular-shifted a spike train 10,000 times and obtained a null distribution for the projection values. Then, the distribution difference between the prior and posterior was computed at each iteration. When the spikes were circularly shifted, the simulated posterior lost the correspondence between stimulus and spike occurrence. Comparing the actual and simulated differences, P values were calculated as a proportion of the fraction of simulated differences that exceeded the actual difference. NLs with $P < 0.01$ were considered significant.

The effect of different stimulus durations for the awake squirrel monkey dataset was assessed by comparing the derived ASI of NLs for the full duration (30 min) with 20 min or 10 min segments containing a part of the 30 min spike train (Friedman test). Particularly, the shortest DMR duration was contrasted to the full duration (Spearman test).

Since firing rates may vary depending on brain states and species, we controlled for the influence of firing rate on ASI by using a resampling procedure. For neurons with firing rates greater than 10 Hz, we down-sampled the distribution of projections corresponding to a spike (posterior distribution) with 2,500 iterations. Since each projection value represents the projection of one stimulus segment that preceded a spike, we randomly selected a subset of projection values so that the number was equal to that of a neuron that fired at 4 Hz, approximately the median of the overall firing rate distribution. We then used this subset of projection values to recalculate the NL and the ASI. We use STA rather than MID1 for the supplemental simulations since repetitive MID estimations are not computationally feasible for iterative procedures.

Data reuse

The data sets of awake and anesthetized squirrel monkeys and awake mice have been newly collected and not published prior to this study. For cats and rats, the data were presented previously for other types of analyses. We recalculated the anesthetized cat data from our previous MID studies that characterized the basic properties of MIDs in the A1 (Atencio et al. 2008, 2009) or compared the MIDs of different auditory stations (Shih et al. 2020). A portion of anesthetized rat data was previously used for evaluating noise exposure effects on A1 STAs (Homma et al. 2020) or comparing the MIDs in A1 and another rat core AC (Homma et al. 2021). We also added data from sixteen new rats to this study, and a part of the new data were used for comparing coordinated neuronal ensemble properties in the AC and thalamus (Hu et al. 2024). None of the data set was published for a multispecies comparison nor focused on the symmetric MID1 NLs.

Results

To explore the factors that shape the NLs in A1 and to determine potential difference and similarity in information processing in different species and brain states, we obtained single units from awake squirrel monkeys ($n = 376$), awake male mice ($n = 283$), awake female mice ($n = 173$), anesthetized squirrel monkeys ($n = 61$), anesthetized cats ($n = 303$), and anesthetized rats ($n = 400$). Anesthesia was mainly maintained by ketamine supplemented with diazepam or xylazine during extracellular recording (see Methods for details). As a sound stimulus, spectro-temporally modulated DMR were presented for 10 to 30 min.

STRF estimation by STA and MID

To assess the influence of the applied derivation method on STRFs and their NL, we used both the STA and MID approaches. In Fig. 1, the STA and the first two MIDs are shown for four neurons from the core AC of awake squirrel monkeys (SqMs) combined with their respective NLs. Filters are displayed in the form of the spectro-temporal stimulus power preceding the occurrence of a spike. NLs relate the match between stimulus and filter to the evoked firing rate. The first two neurons (upper two rows) show a high similarity between the STA filter and the strongest, most informative of the two MID filters (MID1) suggesting that both methods capture closely related aspects of the neurons' stimulus preference. The shape of their NLs is also highly similar, both neurons have asymmetric NL shapes with a high asymmetry index (ASI, see Methods). The filter of the weaker, second MID (MID2) diverges from those of the STA and MID1, capturing a different spectro-temporal stimulus feature that also can activate these neurons. Furthermore, the NL of MID2 invariably is highly symmetric (ASIs near 0), reflecting that both positive and negative correlations between stimulus and filter can elevate the firing rate. These two neurons are representative for the majority of neurons in A1 of anesthetized cats (Atencio et al. 2008, 2009; Shih et al. 2020) and rats (Homma et al. 2021).

The two neurons illustrated in the bottom rows of Fig. 1 differ from the upper two examples in several ways. First, the NLs of both STAs and MID1s are more symmetric, as indicated by lower ASI values. Second, the features of the STAs appear to be noisier and less well defined than for the MID1s as indicated by lower reliability indices (RIs, see Methods). Third, the firing rate for the bottom neuron, as reflected in its STA NL, is reduced relative to the MID1 firing rate. These differences reflect a critical limitation of the STA approach. If a neuron responds to an envelope feature and also to its inverted spectrogram, as indicated by a symmetric NL, the STA averaging process eliminates both versions from the accumulation and creates a weaker estimate of the STRF. By contrast, MIDs can retrieve well defined filters for neurons with asymmetric as well as symmetric NLs (Sharpee et al. 2004).

Nonlinearity shape

We observed clear differences in the distributions of ASIs for the NLs associated with the STA, MID1, and MID2 for the 376 neurons recorded from A1 of awake SqMs (Fig. 2A). Data were combined across all cortical depths since a reliable assignment to specific layers was not feasible in these awake recordings. ASI values were only included if the MID1 NLs were statistically significant at $P < 0.01$ (see Methods). The ASI distributions of the NLs for all

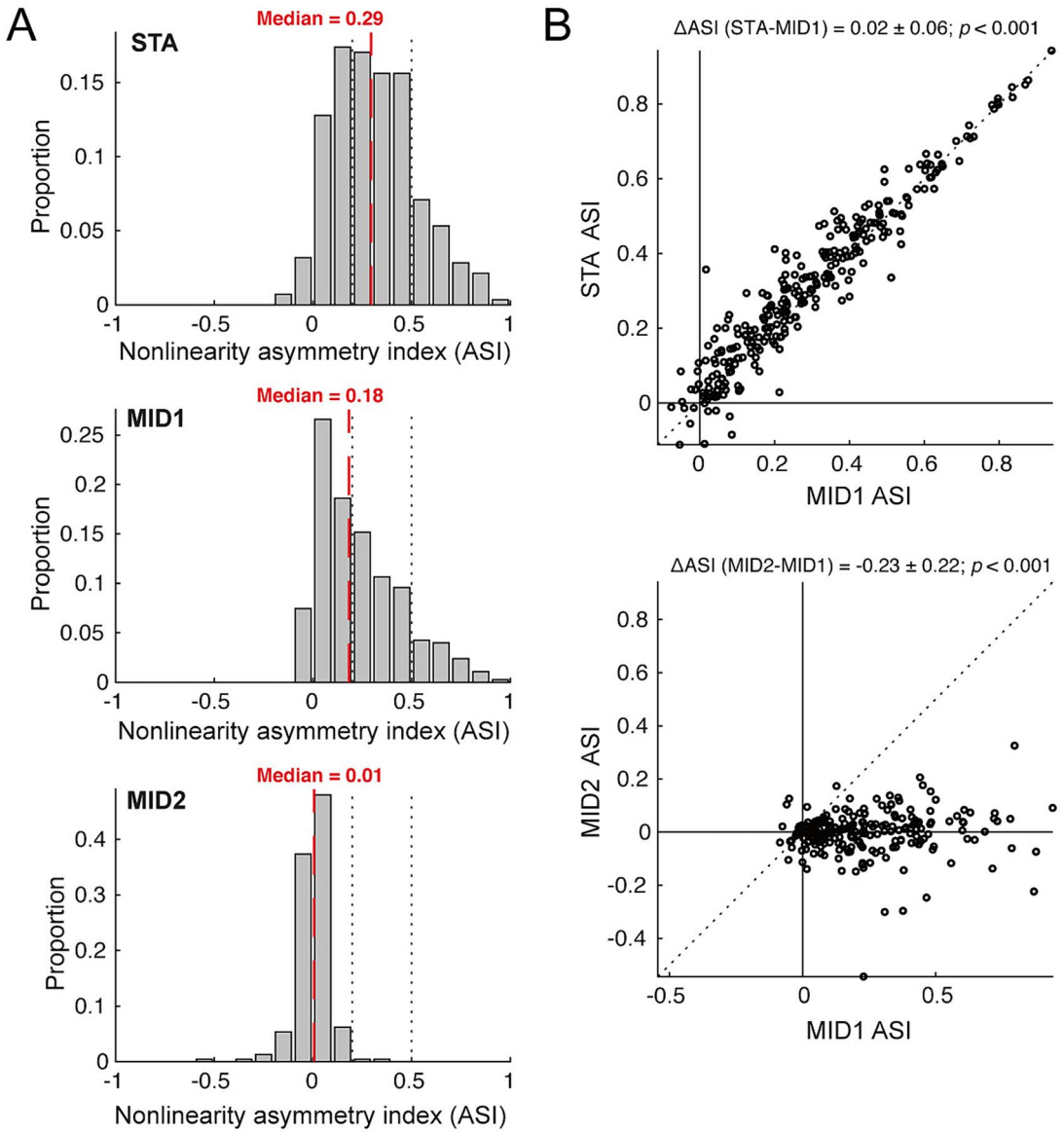

Fig. 2. Distribution of nonlinearity asymmetry index (ASI) in A1 of awake squirrel monkeys. A) ASI proportions for STAs ($n = 282$), MID1s ($n = 376$) and MID2s ($n = 225$). Dotted lines represent the boundaries for the strongly symmetric (ASI < 0.2) and asymmetric nonlinearities (ASI > 0.5). B) Scatter plot of ASIs for STA versus MID1 and MID2 versus MID1. Pairwise differences are indicated at the header. See the Supplemental Table 1 for details of statistical analysis.

derived filters were unimodal. We define strongly asymmetric NLs as an ASI > 0.5 such that the firing rate related to the negative side of the NL is less than 1/3 of the positive side. Conversely, we define strongly symmetric NLs as having an ASI < 0.2, such that 2/3 of the firing rate for the negative side of the NL is larger than the rate of the positive side. The median ASI for STA NLs was 0.29 reflecting a mix of asymmetric and symmetric NLs. Relative to STA NLs, MID1 NLs show a shift toward lower ASIs (median of 0.18), and ~50% of the NLs were strongly symmetric in the awake SqM. Finally, the ASI distribution of MID2 NLs was tightly positioned around ASI = 0 reflecting strongly symmetric NLs for the secondary filter. Despite the shift to lower ASIs for MID1 NLs, STA and MID1 ASIs were highly correlated ($r^2 = 0.95$; $P < 0.001$) and the average pair-wise difference between STA and MID1 ASIs was relatively small (0.02 ± 0.06; $P < 0.001$). By contrast, there appeared to be no relationship between the degree of NL symmetry of MID1 and MID2 (Fig. 2B, bottom panel) and the difference between MID1 and MID2 ASIs was large (-0.23 ± 0.22; $P < 0.001$).

We discussed the data for awake SqMs first since we expect those results to be most representative for human AC. Extending the analysis to the other species and anesthetic states we found some significant differences in the ASI distributions (Fig. 3). Figure 3A shows the distribution of MID1 ASIs for awake SqMs and male/female mice (left three panels), and anesthetized SqMs, cats (data with permission from Atencio et al. 2008, 2009; Shih et al. 2020) and rats (Homma et al. 2021; Hu et al. 2024). ASIs were included for significant NLs at a $P < 0.01$, except for the anesthetized monkey, where we also plotted NLs at $P < 0.05$ due to the lower yield in that group for the plots (although they were not included in the statistical group comparisons). Overall, MID1 ASI values were significantly lower in the awake groups than in the anesthetized groups, indicating a shift toward more symmetric NLs during alertness (Fig. 3B–C). These differences were not

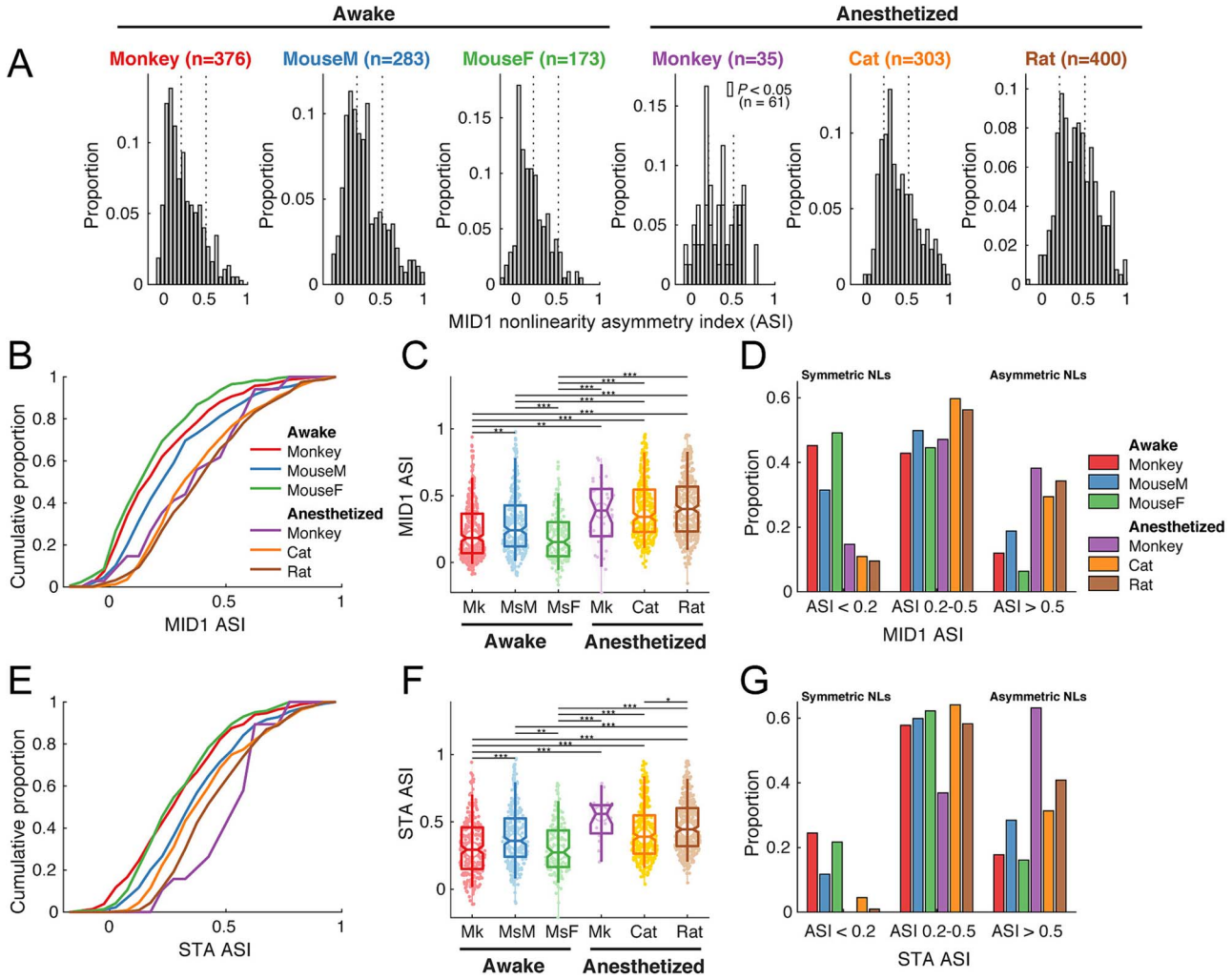

Fig. 3. MID1 ASI values for 6 experimental groups. A) MID1 ASI distributions for significant nonlinearities (NLs) ($P < 0.01$) for awake squirrel monkeys ($n = 376$), awake male mice ($n = 283$), awake female mice ($n = 173$), anesthetized squirrel monkeys ($n = 35$ for NLs of $P < 0.05$, $n = 61$ for NLs of $P < 0.05$), anesthetized cats ($n = 303$), anesthetized rats ($n = 400$). B) Cumulative distributions of MID1 ASIs. C) Box plots of median values plus 25th–75th percentiles of MID1 ASIs with the 5th–95th percentiles depicted by whiskers. Significant statistical differences are indicated by horizontal lines with asterisks. (The box plot presentation is the same for other figures.) D) histogram of the MID1 proportions with strongly symmetric (ASI < 0.2) and asymmetric NLs (ASI > 0.5). E) Cumulative distributions of STA ASIs. F) Box plots for STA ASIs. G) Histogram of the STA proportions of strongly symmetric and asymmetric NLs. (***: $P < 0.001$; **: $P < 0.01$; *: $P < 0.05$).

caused by species differences because awake SqMs also exhibited more symmetric NLs than the anesthetized SqMs, supporting the conclusion of a significant influence of brain state/anesthesia on the expression of symmetric NLs. In addition, although the female mice showed slightly more symmetric NLs than male mice, this sex difference was considerably smaller compared to the difference for brain state/anesthesia.

We summarized the ASI changes by calculating the proportions of strongly symmetric (ASI < 0.2) and strongly asymmetric (ASI > 0.5) MID1 NLs for the six experimental groups (Fig. 3D). Among the awake animals, there was a moderate but significant species difference among the awake animals—awake SqMs and female mice exhibiting ~10% more strongly symmetric NLs (ASI < 0.2) than the awake male mice (Fig. 3C, D). No clear species difference was observed between the MID1 ASI distributions of anesthetized animals (Fig. 3C). For awake animals, the proportion of strongly symmetric NLs exceeded that of strongly asymmetric NLs. This relationship was inverted for anesthetized animals, which showed about twice more asymmetric than symmetric MID1 NLs. About 50% of neurons had intermediate ASI values between 0.2 and 0.5 indicating that they require both linear and quadratic terms to capture the shape of their NLs (Fig. 3D).

A similar picture emerged for the NLs of STAs (Fig. 3E-G) although the proportion of symmetric NLs is drastically reduced, as would be predicted by how STAs are calculated (see Methods). Symmetric STA NLs outnumbered the asymmetric STA NLs only in awake SqMs and mice (Fig. 3G). In anesthetized animals, asymmetric STA NLs substantially exceeded the symmetric NLs (Atencio et al. 2008, 2009; Shih et al. 2020; Homma et al. 2021). Again, the slightly lower number of asymmetric STA NLs for awake male mice indicates a sex difference.

To summarize, for MID1s we observed a clear effect of the brain state (awake versus anesthesia) on the shape of the NL. Awake animals had a higher preponderance of symmetric MID1 NLs than anesthetized animals. Species differences in NL shape distribution were observed between the male mice and the other two awake groups. For STAs, a much smaller proportion of symmetric NLs emerged suggesting that the STA method can only provide a biased and incomplete characterization of cortical NLs.

ASI relationship to STRF properties

Next, we determined whether NL shapes were associated with fundamental receptive field properties, including frequency preference, tuning, and firing rate. The determination of the BF and bandwidth (BW) is illustrated for two A1 neurons, one with symmetric (Fig. 4A) and another with asymmetric NLs (Fig. 4B), obtained from awake SqMs. Recordings in the different species required a focus on different frequency ranges due to differences in their audiograms (Fig. 4C, D). However, no clear dependency of the ASI on the BF was observed for most groups, except for a small increase of ASIs with increasing BF in mice and an opposite small decrease of ASIs with increasing BF in cats (Fig. 4G). There was, however, a clear relationship between NL shapes and sharpness of tuning (Q = BF/BW; Fig. 4A). Although the range of Q differed significantly between the species (Fig. 4E–F), ASIs were significantly correlated with Q for all groups except for the anesthetized SqMs (Fig. 4H). For that group, the lack of statistical significance likely stems from the low cell count when only considering highly significant NLs ($P < 0.01$, $n = 35$). Overall, neurons with narrow frequency tuning (high Q) tended to have more asymmetric NLs, whereas broadly tuned neurons had more symmetric NLs. However, even for sharply tuned neurons there existed a wide range of ASI values, suggesting that frequency bandwidth alone is not the sole determinant of NL shape.

The approaches for STRF and NL estimation depend on firing rate, which can vary widely between neurons (Fig. 5). ASIs exhibited a significant anticorrelation with firing rate for all groups. Generally, neurons with high firing rates tended to have lower ASIs (i.e. more symmetric NLs), compared to neurons with low firing rates. To test whether firing rate is a predictor of ASI, we down-sampled spike trains recorded with firing rates larger than 10 spike/s to the median firing rate of 4 spike/s in awake SqMs (Supplemental Fig. 1). The subsampled spike trains that resulted in significant NLs for both conditions did not show statistically significant ASI differences ($\Delta ASI = -0.02 \pm 0.08$, $P = 0.122$; $n = 18$; Wilcoxon signed-rank test). One potential source of this observation could be cell-type specific differences. For example, inhibitory interneurons, often displaying higher firing rates than pyramidal neurons (Hromádka et al. 2008; Schiff and Reyes 2012), may also express more symmetric NLs.

Similarly, we tested whether the duration of the recorded spike train, which affects the total spike count, influenced ASI values. This is relevant because the different experimental groups were tested with stimulus durations ranging from 10 min (mice) to 30 min (awake SqMs). By subdividing longer spike trains from the awake SqM into 10- and 20-min sections and comparing the ASIs between those condition (Supplemental Fig. 2), we noted a small decrease in ASI value for the 10 min segments ($\Delta ASI = -0.03 \pm 0.12$, $P = 0.009$; $n = 88$; Wilcoxon signed-rank test). Stimulus durations of 20 and 30 min showed no ASI differences.

STRF reliability and MI of LN models

The predictive quality of LN models can be quantified by the MI between a neuron's actual spiking response and the projection values of the stimulus set onto the model filter and NL (e.g. Shih et al. 2020). The amount of captured information, however, is also tied to the quality of the obtained STRFs and can be limited by experimental conditions, such as recording stability and signal-to-noise ratio. The RI quantifies whether STRF samples have a reproducible structure (Escabi et al. 2014; See et al. 2021), and we have extended this procedure to MIDs (Homma et al. 2021) (see Methods). The reliability of MID1 STRFs of awake SqMs was similar to that of anesthetized rats and cats (Fig. 6A-B). RI values of both awake male and female mice, however, were slightly lower than for the anesthetized groups (Fig. 6A-B), but not different from the awake SqM. The MI of MID1s for awake animals was generally higher than for the anesthetized animals (Fig. 6C-D) suggesting increased information throughput in that brain state. A similar trend of increased MI for awake animals was also observed in MID2 information while that was not clear in STA information.

The MID1 ASI was strongly correlated with both RI (Fig. 6E) and MID1 information (Fig. 6F). Asymmetric NLs were associated with the highest reliability as well as highest MI across all groups. For awake animals, neurons with strongly symmetric NLs exhibited a wide range of MI values (Fig. 6F) whereas, for anesthetized animals, symmetric NLs were mostly seen for neurons with low information values. Particularly, awake female mice showed weaker correspondence between NL shapes and MI values. The larger number of symmetric NLs with high MI in the awake animals appears to provide the awake animals with a wider variety of processing options than for anesthetized animals.

MID1 information was found to be significantly higher than STA information for all groups except anesthetized cats and rats (Fig. 7A). The information gain of MID1 over STA was especially clear for the awake animals (SqMs and mice), and more moderate for the anesthetized SqMs (Fig. 7A-B). The relative information gain of MID1s versus STAs, as reflected in the STA/MID1 information ratio, was largest for the awake SqMs (median 73%), followed by the awake female mice (49%), then the anesthetized SqMs (25%) and the awake male mice (16%; Fig. 7C). By contrast, the relative MID1 information gain for anesthetized rats and cats was negligible (− 2–3%, median Δ(MID1-STA) (bits/spike): cats, −0.0017, rats, −0.0014).

A similar comparison between the information of the secondary filter, MID2, versus MID1 (Fig. 7D-F) showed that the MID2 filters captured less absolute information than MID1 in agreement with previous studies (Atencio et al. 2008, 2009; Shih et al. 2020; Homma et al. 2021). However, the relative MID2 information versus MID1 was ∼50% higher for the awake groups (Fig. 7D) than for the anesthetized groups. Thus, the contribution of the secondary STRF component in sound processing is stronger in the awake state.

To summarize, MID1s and MID2s generally captured more information in awake animals than in the anesthetized groups. MID1 information exceeded STA information for all groups except anesthetized cats and rats. The gain of MID1 information over STA was especially pronounced in the awake SqMs. The relative amount of MID2 information versus MID1 information was highest in awake animals boosting its functional relevance. These observations emphasize that the information captured by LN models strongly depends on the brain state of the animal as well as on the derivation methods for the LN components.

Discussion

NLs are a fundamental descriptor of neural processing in the AC and play a critical role in how attributes of complex sounds are extracted and interpreted. In this comparative study of the properties of NLs in linear-nonlinear models of auditory cortical neurons we made the following observations:

(1) In awake animals, the NLs associated with the primary feature filter (MID1) are predominantly symmetric whereas in anesthetized animals MID1 NLs, as a group, are predominantly asymmetric. This suggests that the brain state can influence critical aspect of neuronal function.

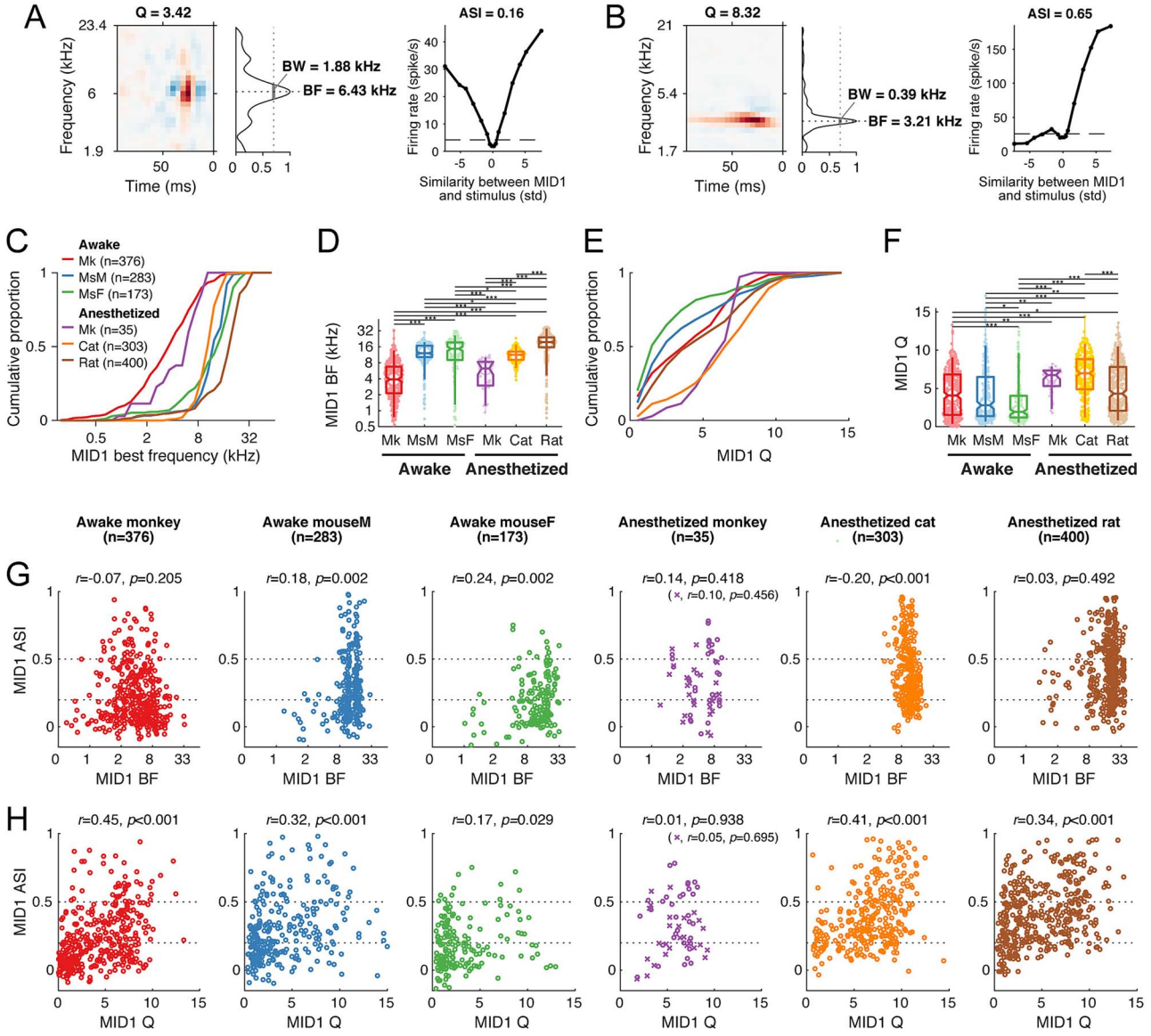

Fig. 4. Relationship of ASIs to spectral tuning properties of MID1 STRFs. A) MID1 STRF and marginal of the frequency profile (rectified, on a log2 scale) for a symmetric NL. Peak: Best frequency (BF). Spectral bandwidth (BW) is measured at the 70% height of the marginal distribution. Q = BF/BW. B) MID1 STRF and marginal of the frequency profile (rectified) for an asymmetric NL. C) Cumulative proportion of BF. D) Boxplot of the MID1 BFs. E) Cumulative proportion of Q values. F) Boxplot of the MID1 Q. G) Scatter plots of MID1 ASI versus BF. Circles: NL significance: $P < 0.01$; crosses: $P < 0.05$. Correlation coefficient and p-values are indicated at the header. H) Scatter plots of MID1 ASI versus sharpness of tuning (Q). Dotted lines in 4G and 4H represent the boundaries for the strongly symmetric (ASI < 0.2) and asymmetric nonlinearities (ASI > 0.5). (***: $P < 0.001$; **: $P < 0.01$; *: $P < 0.05$).

(2) Awake SqMs and female mice have a higher proportion of symmetric MID1 NLs than awake male mice. By contrast, the proportion of symmetric NLs among the species in the anesthetized group are fairly similar. This indicates the presence of some sex and, potentially, species differences in cortical processing.

(3) The degree of MID1 NL asymmetry is correlated with the neuron's sharpness of frequency tuning. This suggests specific relationships between filter properties and aspects of their corresponding input/output functions.

Together, these observations provide evidence that the cortical processing of sound is more complex and varied in awake versus anesthetized animals. The shift toward more symmetric NLs in awake animals potentially may indicate an increase of the tolerance for—or invariance to—some spectral envelope features. The increased variety in MID1 NL shape and stronger MID2 filters can provide a broad algorithmic repertoire for cortical sound processing in awake animals.

Methodological considerations

Before considering the interpretation and potential functional implications of these findings, we will briefly discuss some methodological aspects that could potentially limit the generality of our findings.

Synthetic stimuli, like the DMR, contain essential properties of natural sounds and can serve as effective tools for estimating the response properties of auditory neurons (Escabi and Schreiner 2002; Atencio and Schreiner 2013). The DMR stimuli used in this study were nearly identical for the different experimental groups regarding bandwidth, intensity, depth of modulation, and range of spectral modulations. Nevertheless, stimulation with DMRs did vary in a few aspects. First, we used a wider range of temporal modulations in the awake and anesthetized SqM (a maximum of 64 or 150 Hz compared to 40 Hz in mice, cats, and rats) due to the fact that cortical neurons in New World primates process a wider range of temporal modulations than in carnivores and

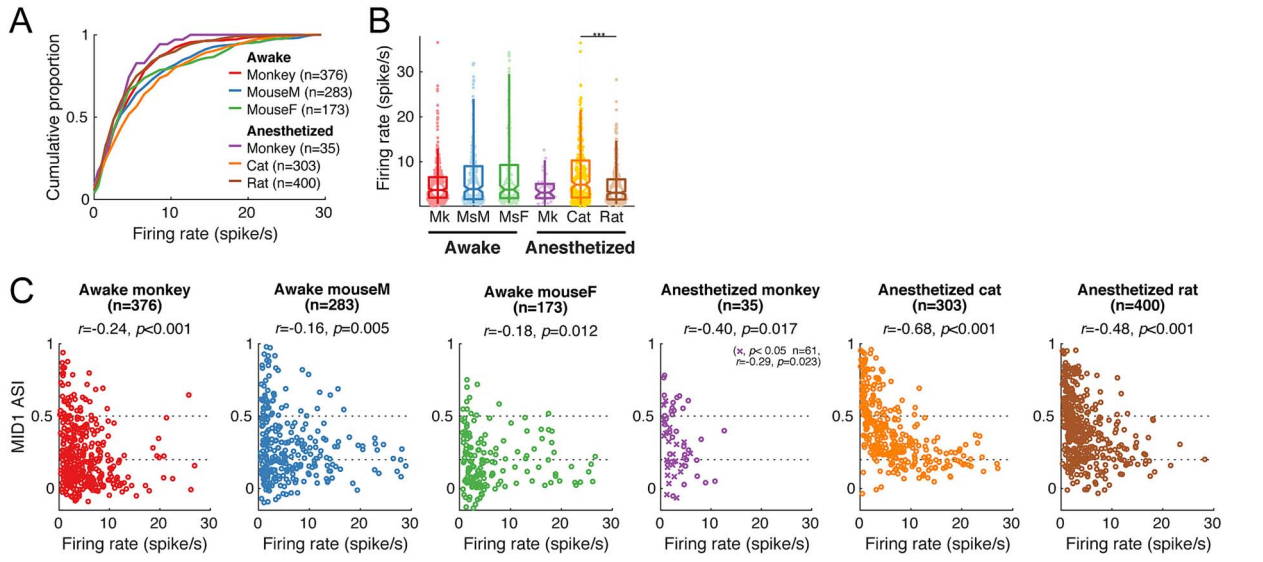

Fig. 5. Relationship between firing rate and MID1 ASI. A) Cumulative distributions of firing rate. B) Box plots for firing rate. (comparisons for significant NLs at $P < 0.01$; ***: $P < 0.001$). C) Scatter plots of MID1 ASI versus firing rate. Circles: NL significance: $P < 0.01$; crosses: $P < 0.05$. Correlation coefficient and p-values are indicated.

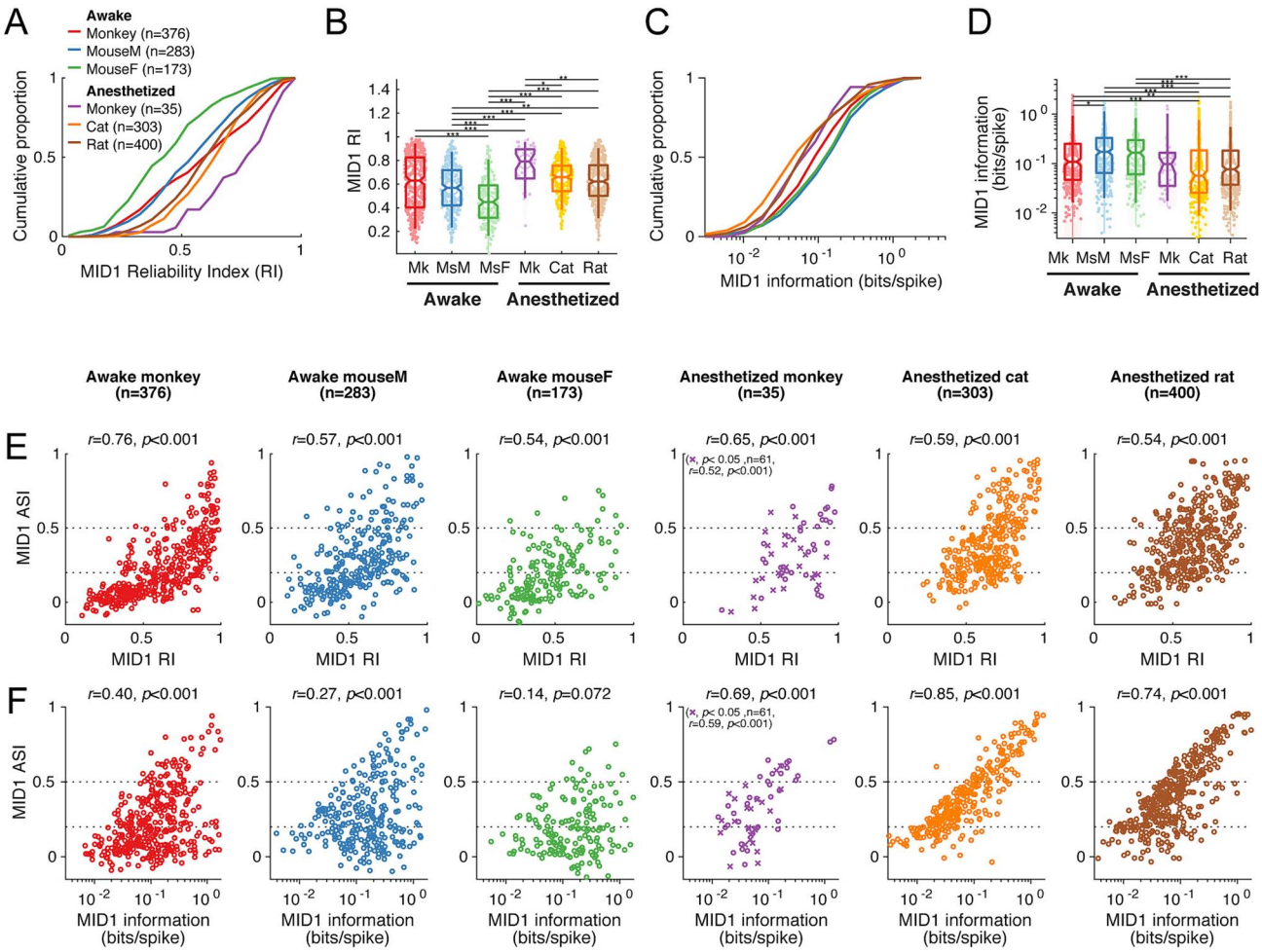

Fig. 6. MID1 STRF reliability and information content. A) Cumulative distributions of MID1 RI, a measure of the STRF repeatability. B) Box plots for RIs. C) Cumulative distributions of the mutual information ("information") between stimulus and predicted spike train for MID1 STRFs with associated NLs. D) Box plots for the MID1 information. E) Scatter plots of MID1 ASI versus MID1 RI. F) Scatter plots of MID1 ASI versus MID1 information. (comparisons for significant NLs at $P < 0.01$; ***: $P < 0.001$; **: $P < 0.01$; *: $P < 0.05$).

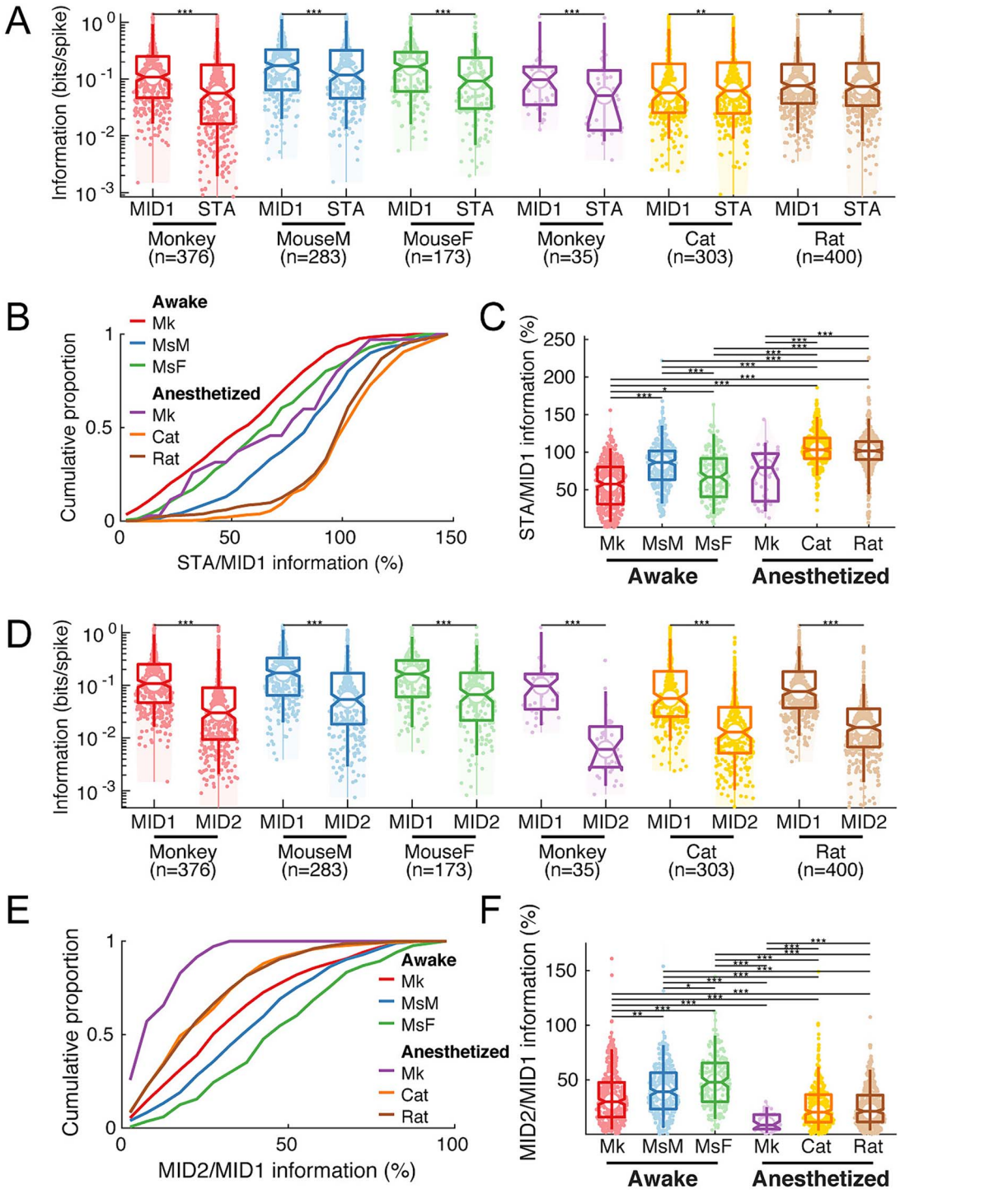

Fig. 7. Information relationship between STA, MID1, and MID2. A) Box plots for MID1 and STA mutual information with paired comparisons between the two filters. B) Cumulative distributions of the information ratio STA/MID1. C) Box plots for STA/MID1 information ratio. D) Box plots for MID1 and MID2 mutual information. E) Cumulative distributions of information ratio MID2/MID1. F) Box plots for MID2/MID1 information ratio. (***: $P < 0.001$; **: $P < 0.01$; *: $P < 0.05$).

rodents (Bieser and Müller-Preuss 1996; Hoglen et al. 2018; Lu et al. 2001; Malone et al. 2013; Martin et al. 2017). It is unlikely, however, that including higher temporal modulations will strongly bias either the obtained filters or NLs, because modulations below 32 Hz dominate the responses in all tested species (Atencio and Schreiner 2010, 2012; Malone et al. 2013; Hoglen et al. 2018; Homma et al. 2020).

Second, in the awake animals, free field sounds provided binaural stimulation, whereas sounds in the anesthetized animals were delivered monaurally to the contralateral ear. While the role of binaural interactions on the shape of filters and NLs has not been sufficiently explored for the cortex, previous studies in the inferior colliculus indicate that the contra- and ipsi-STRFs can be distinctly different and systematic differences in the

converging receptive field structures may account for some binaural sensitivities (Qiu et al. 2003). It can, therefore, not be ruled out that monaural versus binaural stimulation may have an effect on the observed structure of NLs.

Third, the stimulus duration differed between the experimental groups. The duration, chosen based on other, unrelated experimental criteria, varied between 10 min in mice to 30 min in SqMs. Comparing NLs obtained from subsampled 10 min DMR segments to segments of 20- or 30-min durations from the same neuron showed a small but statistically significant influence of stimulus duration on the filters or NL shape. However, the similar MID1 ASI values obtained for long-duration monkey versus short duration female mice recordings in awake animals suggest that recording duration by itself had no major influence on the conclusions.

Fourth, the array electrodes varied from 16 channels and length of 2.25 mm in cats to 32 or 64 channels over 1.3 mm in the other species. Recordings with the shorter electrode array may have caused an undersampling of deep layer 6 and/or shallow layer 2. However, comparing cat MID1 ASI values, predominantly obtained with 16-channel electrodes, and anesthetized rat and squirrel monkey data, predominantly obtained with 32 and 64 channels, showed no statistically significant difference (Fig. 3C).

Shape of NLs

In the context of linear-nonlinear models, the way sensory cortical neurons process sensory information can reflect differences in the receptive field structure embodied in the filters, as well as differences in the associated NLs, as has been demonstrated for the visual system (e.g. Pollen et al. 1988; Rust et al. 2005; Chen et al. 2007; Kastner and Baccus 2011). Previously, no comprehensive assessment of the properties of auditory cortical NLs in awake mammals had been available. Here, we demonstrate that the dominant filter (MID1) for A1 neurons exhibited a wide range of NL shapes, from strongly asymmetric to fully symmetric, particularly in awake animals. The distribution of ASIs were unimodal in both awake SqMs and mice, reflecting an underlying continuum in the degree of stimulus-filter correlations that govern firing rates. Neurons with asymmetric NLs fire in proportion to the degree of positive stimulus-filter matches, a characteristics of simple feature detectors. Neurons with symmetric NLs, by contrast, tolerate certain variations in the stimulus, such that both high positive and negative correlations with the filter can elevate firing rates. The wide distribution of ASIs indicates that cortical neurons exhibit a significant diversity of NL shapes (see Fig. 1). In awake animals, neurons that contain some symmetry or quadratic aspects in their NLs (ASI < 0.5) constitute nearly 80% of the population. This implies that the majority of A1 neurons exhibit some tolerance to certain stimulus variations and only ~20% of the population operate as variation-intolerant feature detectors.

The NLs of the secondary, weaker MID2 filter are universally strongly symmetric; therefore, they are tolerant of phase variations in the stimulus envelope, indicating that the two main filters of A1 neurons can follow different principles for implementing information processing.

A similar distinction of neurons best modeled with either symmetric or asymmetric NLs has been made for the visual cortex (Hubel and Wiesel 1962; Dean and Tolhurst 1983). There, "simple" cells have asymmetric NLs, characteristic of feature detectors, while "complex" cells with symmetric NLs exhibit a high degree of stimulus position tolerance as indicated by their low F1/F0 ratio in response to spatial gratings for both awake and anesthetized animals (Skottun et al. 1991; Mechler and Ringach 2002; Priebe et al. 2004; Vintch et al. 2015). A similarly broad distribution of NL shapes had not been seen for primary filters (MID1) in A1 of anesthetized animals (Atencio et al. 2008, 2009; Shih et al. 2020). These initial auditory studies under anesthesia appear to have underestimated the diversity of NL shapes. Our observation of a broad variety of NL shapes in A1 of alert animals suggests the presence of similar processing principle in visual and auditory cortices.

STA NLs also show a range of shapes between strongly symmetric and asymmetric, similar to the properties of MID1 NLs, although the proportion of strongly symmetric STA NLs was greatly reduced (Fig. 3). Due to the linear averaging of stimuli in the generation of STAs, pairs of spike-eliciting stimuli with envelope phase differences near 180° effectively cancel each other out for neurons with symmetric MID1 NLs and weakens the representation of preferred stimulus features in their STRFs (Fig. 1). The prevalence of strongly or moderately symmetric MID1 NLs in the awake preparation demonstrates how the use of the STA methods may lead to misrepresentations of the actual spectro-temporal properties of neurons (Atencio and Schreiner 2013; Atencio et al. 2008, 2012, 2017; Shih et al. 2020).

NL shape did not appear to be BF dependent in the examined species, but a moderate relationship with STRF bandwidth was observed in all experimental groups. Wider filter bandwidths yielded more symmetric NLs with potentially increased tolerance of stimulus changes, such as a frequency shift in the envelope.

Neurons with higher firing rates tended to have lower ASI values for MID1s in all four species, i.e. their NLs tend to be more symmetric (Fig. 5). Down-sampling of the higher firing rate (from >10 to 4 spike/s) did not result in a significant change in ASI. Therefore, firing rate alone is not a strong predictor of NL shape. The reason why high-rate neurons show lower ASIs is not obvious. However, complex cells in visual cortex also tend to have higher firing rates than simple cells (e.g. Duysens et al. 1982), potentially a consequence of stronger recurrent inputs of the former (Sakai and Tanaka 2000; Boutin et al. 2002). This may reflect potential circuit commonalities between the two modalities.

Sex differences in auditory function of rodents are prevalent and influenced by multiple factors including physiological mechanisms, anatomical variations, and behavioral performances (Lin et al. 2022; Calhoun et al. 2023; Guma et al. 2023). However, there is little evidence of distinct cellular sex differences in auditory cortical neurons. Our observation of differences in the NL symmetry between male and female mice suggests that role-specific adaptations do exist as has been demonstrated for differences in temporal processing between mothers and virgin mice (Liu et al. 2006; Liu and Schreiner 2007).

Effects of anesthesia

NL symmetry in A1 neurons was clearly affected by brain state (Fig. 3B-D), such that, across species, awake animals had significantly more symmetrical NLs than anesthetized animals. This was also confirmed by comparing awake and anesthetized animals in the same species, the squirrel monkey, although the statistical power in that comparison was reduced due to the low number of highly significant cells in the anesthetized condition. Additionally, the total MI obtained for both MID filters in awake animals exceeded that of the anesthetized animals indicating that anesthesia substantially reduces the expression of the integrative complexity of cortical STRFs.

Ketamine, a N-methyl-D-aspartate (NMDA) receptor antagonist, was the main anesthetic agent used here, in combination with either xylazine or diazepam. Adding diazepam (cats) or xylazine (rats, SqMs) to ketamine did not produce consistent differences in our results. While anesthesia has complex effects

on auditory cortical processing (Gaese and Ostwald 2001; Heinke and Koelsch 2005; Syka et al. 2005; Zhang et al. 2014; Cheung et al. 2001; Schaefer et al. 2017; López-Jury et al. 2023), the specific effects of ketamine on cortical function are not fully understood. Tangible influences of ketamine anesthesia on basic STRF properties, such as amplitude modulation preference or frequency tuning, appear to be quite modest (Walker et al. 2008; Guo et al. 2012; Zhang et al. 2014; Miller et al. 2016; Martin et al. 2017). Reduced coupling of excitatory and inhibitory input circuits under ketamine has been hypothesized to affect recurrent excitation (Deane et al. 2020) as well as pre- and postsynaptic adaptation (López-Jury et al. 2023). A lack of inhibitory modulations from supragranular populations on recurrent excitation has also been reported (Wehr and Zador 2003; Kato et al. 2017) suggesting that ketamine can influence both local circuits and long-range recurrent networks.

In the visual cortex, experimental reduction of recurrent inputs resulted in a conversion of complex cells (with symmetric NLs) into simple-like cells (with asymmetric NLs; Bardy et al. 2006) as has been postulated from computational modeling (Chance et al. 1999). This suggests that the relative lack of symmetric NLs in A1 under ketamine may reflect a reduction of recurrent inputs. Thus, the generation of and distinction between symmetric and asymmetric NLs in A1 and visual cortex may reflect canonical principles in cortical processing across modalities.

Neurons with symmetric MID1 NLs likely integrate both local and distant input projections from neurons possessing a wider range of NL shapes, more variable feature filters, or both. By analogy to the proposed generation of complex cells in visual cortex (Marr et al. 1980; Chance et al. 1999; Sakai and Tanaka 2000; Lian et al. 2021; Boutin et al. 2002), neurons with symmetric MID1 NLs may receive inputs from neurons with complementary filters that are phase shifted by 90° or 180°. The Gabor model of visual complex cells requires two filters in quadrature phase to achieve phase invariant tuning (Marr et al. 1980). Further studies are required to reveal the integration principles of auditory cortical neurons.

Functional roles of symmetric and asymmetric NLs

An important functional characteristic of complex cells in visual cortex is their invariance to spatial image translation on the retina as exemplified by strong responses evoked by oriented gratings for a wide range of spatial phases (Skottun et al. 1991). This property distinguishes them from simple cells, whose responses are highly selective for the spatial phase of gratings, and intolerant to image translation more generally. We predict from our results that auditory cortical neurons with different NL shapes can serve purposes similar to their visual counterparts, including translational invariance. For auditory neurons, translation invariance across the receptor surface would apply to a frequency shift of the spectral envelope of a complex sound. An example is the shift of vowel formant frequencies when uttered by speakers with different vocal tract length. The formant frequencies of women and children are shifted to higher frequencies relative to male speakers (e.g. Zahorian and Jagharghi 1993; Supplemental Fig. 3A-B). However, the relative distance of the spectral envelope peaks or valleys of a given vowel remain relatively constant when expressed in terms of ripple density (measured in peaks/octave; Supplemental Fig. 3C). Neurons with a symmetric NL that are tuned to a preferred ripple density are, therefore, expected to show greater tolerance for spectral envelope translation. Those neurons would respond similarly to the same vowels produced for different vocal tract lengths. One would also expect that the response of a neuron with symmetric NL to a spectral envelope grating (or ripple) of fixed density presented at various phases would result in an approximately circular phase response distribution. Illustrative examples of the expected phase distribution for two neurons with symmetric and asymmetric NLs, respectively, obtained from A1 of an awake SqM do illustrate that these response behaviors exist (Supplemental Fig. 3D-E; see legend for details).

A previous study has compared the properties of some auditory cortical neurons to complex cells in the visual system (Tian et al. 2013; Rauschecker 2015). In particular, differences in the spectral profiles of On and Off responses of auditory cortical receptive fields were interpreted to be analogous to the properties of On and Off responses in visual complex cells (Tian et al. 2013; Rauschecker 2015; but see Ramamurthy and Recanzone 2017; Malone et al. 2015). A systematic relationship of auditory On and Off responses and cortical NL shapes, however, has not been established. Here, we propose a broader interpretational framework that potentially unifies functional neuron types across modalities.

Visual complex cells, modeled with symmetric NLs (Fitzgerald et al. 2011; Touryan et al. 2002; Sharpee 2013; Vintch et al. 2015), are involved in a wide range of tasks that can contribute to object recognition. In addition to lacking sensitivity to spatial phase or position (Movshon et al. 1978; De Valois et al. 1982; Pollen and Ronner 1982; Skottun et al. 1991) they have been implicated in processing of stimulus magnitude (Adelson and Bergen 1985), contrast (Mechler et al. 1998; Gawne 2000), textures (Freeman et al. 2013; Kodama et al. 2022), and binaural disparity (Ohzawa et al. 1997), providing the recognition system with robustness to changes in illumination, background, distance, and small spatial distortions (Shams and von der Malsburg 2002; Felsen et al. 2005). It remains to be determined whether and how auditory cortical neurons with symmetric NLs similarly are affecting numerous aspects of auditory cortical processing.

Conclusions

In awake animals, we have found a preponderance of auditory cortical neurons with symmetric NLs, in contrast to previous results in anesthetized animals. We also observed some sex differences in the distribution of NL properties in AC of awake male and female animals, which potentially reflect the unique auditory needs and corresponding cortical processing abilities of maternal vs. paternal roles. The bases of these differences, related to connectional, cellular, and molecular aspects require further studies.

The observed diversity of NL shapes reveals a rich potential resource of computations in AC that may contribute to robust object recognition performance. This emphasizes the need to understand both feature sensitivity and nonlinear input/output functions to characterize the wide range of functional neuronal properties expressed in AC. It also suggests that potential analogous functional processing mechanisms have developed across sensory modalities.

Acknowledgments

We wish to thank Wenxin Hu for help in analysis.

Author contributions

Natsumi Y. Homma (Investigation, Data curation, Formal analysis, Visualization, Software, Validation, Writing—original

draft, Writing—review & editing), Jermyn Z. See (Methodology, Data curation, Software, Formal analysis, Validation), Craig A. Atencio (Methodology, Data curation, Formal analysis, Software, Validation), Congcong Hu (Investigation, Data curation), Joshua D. Downer (Data curation), Ralph E. Beitel (Resources), Steven W. Cheung (Resources), Mina Sadeghi Najafabadi (Data curation), Timothy Olsen (Data curation, Investigation), James Bigelow (Data curation, Investigation), Andrea R. Hasenstaub (Project administration, Funding acquisition, Writing—review & editing), Brian J. Malone (Data curation, Funding acquisition, Writing—review & editing),Christoph E. Schreiner (Conceptualization, Methodology, Investigation, Data curation, Funding acquisition, Project administration, Supervision, Validation, Writing—original draft, Writing—review & editing).

Supplementary material

Supplementary material is available at *Cerebral Cortex* online.

Funding

This work was supported by the National Institutes of Health (DC002260 and DC017396 to C.E.S., DC011843 to B.J.M., DC016535 to J.D., DC016846 to J.B., and DC014101, NS116598, MH122478, and EY025174 to A.R.H.), the Klingenstein Foundation (A.R.H.), PBBR Breakthrough Fund (A.R.H.), the Coleman Memorial Fund (A.R.H., C.E.S.), Hearing Research Inc. (C.E.S., B.J.M., A.R.H), and the Japan Society for the Promotion of Science (N.Y.H.).

Conflict of interest statement: None declared.

References

Adelson EH, Bergen JR. Spatiotemporal energy models for the perception of motion. *J Opt Soc Am A Opt Image Sci Vis*. 1985:2:284–299. https://doi.org/10.1364/JOSAA.2.000284.

Aertsen AM, Johannesma PI. The spectro-temporal receptive field. A functional characteristic of auditory neurons. *Biol Cybern*. 1981:42:133–143. https://doi.org/10.1007/BF00336731.

Agüera Y, Arcas B, Fairhall AL, Bialek W. Computation in a single neuron: Hodgkin and Huxley revisited. *Neural Comput*. 2003:15:1715–1749. https://doi.org/10.1162/08997660360675017.

Ahrens MB, Linden JF, Sahani M. Nonlinearities and contextual influences in auditory cortical responses modeled with multilinear spectro-temporal methods. *J Neurosci*. 2008:28:1929–1942. https://doi.org/10.1523/JNEUROSCI.3377-07.2008.

Atencio CA, Schreiner CE. Columnar connectivity and laminar processing in cat primary auditory cortex. *PLoS One*. 2010:5:e9521. https://doi.org/10.1371/journal.pone.0009521.

Atencio CA, Schreiner CE. Spectro-temporal processing in spectral tuning modules of cat primary auditory cortex. *PLoS One*. 2012:7:e31537. https://doi.org/10.1371/journal.pone.0031537.

Atencio CA, Schreiner CE. Stimulus choices for spike-triggered receptive field analysis. In: Depireux DA, Elihali M, editors. *Handbook of modern techniques in auditory cortex*. New York: Nova Biomedical; 2013, pp. 61–100.

Atencio CA, Sharpee T, Schreiner CE. Cooperative nonlinearities in auditory cortical neurons. *Neuron*. 2008:58(6):956–966. https://doi.org/10.1016/j.neuron.2008.04.026.

Atencio CA, Sharpee T, Sharpee T, Schreiner CE. Hierarchical computation in the canonical auditory cortical circuit. *Proc Natl Acad Sci USA*. 2009:106(51):21894–21899. https://doi.org/10.1073/pnas.0908383106.

Atencio CA, Sharpee TO, Schreiner CE. Receptive field dimensionality increases from the auditory midbrain to cortex. *J Neurophysiol*. 2012:107:2594–2603. https://doi.org/10.1152/jn.01025.2011.

Atencio CA, Sharpee T, Sharpee T. Multidimensional receptive field processing by cat primary auditory cortical neurons. *Neuroscience*. 2017:359:130–141. https://doi.org/10.1016/j.neuroscience.2017.07.003.

Bardy C, Huang JY, Wang C, FitzGibbon T, Dreher B. 'Simplification' of responses of complex cells in cat striate cortex: suppressive surrounds and 'feedback' inactivation. *J Physiol*. 2006:574:731–750. https://doi.org/10.1113/jphysiol.2006.110320.

Bieser A, Müller-Preuss P. Auditory responsive cortex in the squirrel monkey: neural responses to amplitude-modulated sounds. *Exp Brain Res*. 1996:108:273–284.

Bigelow J, Morrill RJ, Dekloe J, Hasenstaub AR. Movement and VIP interneuron activation differentially modulate encoding in mouse auditory cortex. *eNeuro*. 2019:6:0164–0119. https://doi.org/10.1523/ENEURO.0164-19.2019.

Boutin V, Franciosini A, Chavane F, Perrinet LU. Pooling strategies in V1 can account for the functional and structural diversity across species. *PLoS Comput Biol*. 2002:18:e1010270. https://doi.org/10.1371/journal.pcbi.1010270.

Calhoun G, Chen C-T, Kanold PO. Bilateral widefield calcium imaging reveals circuit asymmetries and lateralized functional activation of the mouse auditory cortex. *Proc Natl Acad Sci USA*. 2023:120:e2219340120. https://doi.org/10.1073/pnas.2219340120.

Chance FS, Nelson SB, Abbott LF. Complex cells as cortically amplified simple cells. *Nat Neurosci*. 1999:2:277–282. https://doi.org/10.1038/6381.

Chen X, Han F, Poo MM, Dan Y. Excitatory and suppressive receptive field subunits in awake monkey primary visual cortex (V1). *Proc Natl Acad Sci USA*. 2007:104:19120–19125. https://doi.org/10.1073/pnas.0706938104.

Cheung SW, Nagarajan SS, Bedenbaugh PH, Schreiner CE, Wang X, Wong A. Auditory cortical neuron response differences under isoflurane versus pentobarbital anesthesia. *Hear Res*. 2001:156:115–127. https://doi.org/10.1016/S0378-5955(01)00272-6.

Chichilnisky J. A simple white noise analysis of neuronal light responses. *Network*. 2001:12:199–213. https://doi.org/10.1080/713663221.

Christianson GB, Sahani M, Linden JF. The consequences of response nonlinearities for interpretation of spectro-temporal receptive fields. *J Neurosci*. 2008:28:446–455. https://doi.org/10.1523/JNEUROSCI.1775-07.2007.

Chung JE, Magland JF, Barnett AH, Tolosa VM, Tooker AC, Lee KY, Shah KG, Felix SH, Frank LM, Greengard LF. A fully automated approach to spike sorting. *Neuron*. 2017:95:1381–1394.e6. https://doi.org/10.1016/j.neuron.2017.08.030.

David SV. Incorporating behavioral and sensory context into spectro-temporal models of auditory encoding. *Hear Res*. 2018:360:107–123. https://doi.org/10.1016/j.heares.2017.12.021.

Dayan P, Abbott LF. *Theoretical neuroscience: computational and mathematical Modeling of neural systems*. Cambridge (MA): MIT Press; 2001, p. 2001.

De Valois RL, Albrecht DG, Thorell LG. Spatial frequency selectivity of cells in macaque visual cortex. *Vis Res*. 1982:22(5):545–559. https://doi.org/10.1016/0042-6989(82)90113-4.

Dean AF, Tolhurst DJ. On the distinctness of simple and complex cells in the visual cortex of the cat. *J Physiol*. 1983:344:305–325. https://doi.org/10.1113/jphysiol.1983.sp014941.

Deane KE, MGK B, Curran AW, Zempeltzi MM, Ma J, Lin X, Abela F, Aksit S, Deliano M, Deliano M, et al. Ketamine anaesthesia

induces gain enhancement via recurrent excitation in granular input layers of the auditory cortex. *J Physiol*. 2020:598:2741–2755.
Downer JD, Niwa M, Sutter ML. Task engagement selectively modulates neural correlations in primary auditory cortex. *J Neurosci*. 2015:35:7565–7574. https://doi.org/10.1523/JNEUROSCI.4094-14.2015.
Duysens J, Orban GA, van der Glas HW, Maes H. Receptive field structure of area 19 as compared to area 17 of the cat. *Brain Res*. 1982:23:293–308. https://doi.org/10.1016/0006-8993(82)90367-5.
Efron B, Tibshirani RJ. *An introduction to the bootstrap*. Boca Raton: Chapman and Hall/CRC; 1994.
Elgueda D, Duque D, Radtke-Schuller S, Yin P, David SV, Shamma SA, Fritz JB. State-dependent encoding of sound and behavioral meaning in a tertiary region of the ferret auditory cortex. *Nat Neurosci*. 2019:22:447–459. https://doi.org/10.1038/s41593-018-0317-8.
Escabi MA, Schreiner CE. Nonlinear spectro-temporal sound analysis by neurons in the auditory midbrain. *J Neurosci*. 2002:22:4114–4131. https://doi.org/10.1523/JNEUROSCI.22-10-04114.2002.
Escabi MA, Miller LM, Read HL, Schreiner CE. Naturalistic auditory contrast improves spectrotemporal coding in the cat inferior colliculus. *J Neurosci*. 2003:23:11489–11504. https://doi.org/10.1523/JNEUROSCI.23-37-11489.2003.
Escabi MA, Read HL, Viventi J, Kim DH, Higgins NC, Storace DA, Liu ASK, Gifford AM, Burke JF, Campisi M, et al. A high-density, high-channel count, multiplexed μECoG array for auditory-cortex recordings. *J Neurophysiol*. 2014:112:1566–1583. https://doi.org/10.1152/jn.00179.2013.
Felsen G, Touryan J, Han F, Dan Y. Cortical sensitivity to visual features in natural scenes. *PLoS Biol*. 2005:3:e342. https://doi.org/10.1371/journal.pbio.0030342.
Fitzgerald JD, Rowekamp RJ, Sincich LC, Sharpee TO. Second order dimensionality reduction using minimum and maximum mutual information models. *PLoS Comput Biol*. 2011:7:e1002249. https://doi.org/10.1371/journal.pcbi.1002249.
Freeman J, Ziemba CM, Heeger DJ, Simoncelli EP, Movshon JA. A functional and perceptual signature of the second visual area in primates. *Nat Neurosci*. 2013:16:974–981. https://doi.org/10.1038/nn.3402.
Fritz JB, Elhilali M, Shamma SA. Differential dynamic plasticity of A1 receptive fields during multiple spectral tasks. *J Neurosci*. 2005:25:7623–7635. https://doi.org/10.1523/JNEUROSCI.1318-05.2005.
Gaese BH, Ostwald J. Anesthesia changes frequency tuning of neurons in the rat primary auditory cortex. *J Neurophysiol*. 2001:86:1062–1066. https://doi.org/10.1152/jn.2001.86.2.1062.
Gawne TJ. The simultaneous coding of orientation and contrast in the responses of V1 complex cells. *Exp Brain Res*. 2000:133:293–302. https://doi.org/10.1007/s002210000381.
Guma E, Beauchamp A, Liu S, Levitis E, Ellegood J, Pham L, Mars RB, Raznahan A, Lerch JP. Comparative neuroimaging of sex differences in human and mouse brain anatomy. bioRxiv [Preprint]. 2023:08.23.554334.
Guo W, Chambers AR, Darrow KN, Hancock KE, Shinn-Cunningham BG, Polley DB. Robustness of cortical topography across fields, laminae, anesthetic states, and neurophysiological signal types. *J Neurosci*. 2012:32:9159–9172. https://doi.org/10.1523/JNEUROSCI.0065-12.2012.
Hackett TA, Preuss TM, Kaas JH. Architectonic identification of the core region in auditory cortex of macaques, chimpanzees, and humans. *J Comp Neurol*. 2001:441:197–222. https://doi.org/10.1002/cne.1407.
Heinke W, Koelsch S. The effects of anesthetics on brain activity and cognitive function. *Curr Opin Anaesthesiology*. 2005:18:625–631. https://doi.org/10.1097/01.aco.0000189879.67092.12.
Hoglen NEG, Larimer P, Phillips EAK, Malone BJ, Hasenstaub AR. Amplitude modulation coding in awake mice and squirrel monkeys. *J Neurophysiol*. 2018:119:1753–1766. https://doi.org/10.1152/jn.00101.2017.
Homma NY, Hullett PW, Atencio CA, Schreiner CE. Auditory cortical plasticity dependent on environmental noise statistics. *Cell Rep*. 2020:30:4445–4458.e5. https://doi.org/10.1016/j.celrep.2020.03.014.
Homma NY, Atencio CA, Schreiner CE. Plasticity of multidimensional receptive fields in Core rat auditory cortex directed by sound statistics. *Neuroscience*. 2021:467:150–170. https://doi.org/10.1016/j.neuroscience.2021.04.028.
Hromádka T, Deweese MR, Zador AM. Sparse representation of sounds in the unanesthetized auditory cortex *PLoS Biol*. 2008:e16. https://doi.org/10.1371/journal.pbio.0060016.
Hu C, Hasenstaub AR, Schreiner CE. Basic properties of coordinated neuronal ensembles in the auditory thalamus. *J Neurosci*. 2024:44:e1729232024. https://doi.org/10.1523/JNEUROSCI.1729-23.2024.
Hubel DH, Wiesel TN. Receptive fields, binocular interaction and functional architecture in the cat's visual cortex. *J Physiol Lond*. 1962:160:106–154. https://doi.org/10.1113/jphysiol.1962.sp006837.
Kastner DB, Baccus SA. Coordinated dynamic encoding in the retina using opposing forms of plasticity. *Nat Neurosci*. 2011:14:1317–1322. https://doi.org/10.1038/nn.2906.
Kato HK, Asinof SK, Isaacson JS. Network-level control of frequency tuning in auditory cortex. *Neuron*. 2017:95:412–423.e4. https://doi.org/10.1016/j.neuron.2017.06.019.
Klein DJ, Depireux DA, Simon JZ, Shamma SA. Robust spectrotemporal reverse correlation for the auditory system: optimizing stimulus design. *J Comput Neurosci*. 2000:9:85–111. https://doi.org/10.1023/A:1008990412183.
Kodama A, Kimura K, Sakai K. Dimensionality of the intermediate-level representation of shape and texture in monkey V4. *Neural Netw*. 2022:153:444–449. https://doi.org/10.1016/j.neunet.2022.06.027.
Kouh M, Poggio T. A canonical neural circuit for cortical nonlinear operations. *Neural Comput*. 2008:1427–1451. https://doi.org/10.1162/neco.2008.02-07-466.
Kvale MN, Schreiner CE. Short-term adaptation of auditory receptive fields to dynamic stimuli. *J Neurophysiol*. 2004:91:604–612. https://doi.org/10.1152/jn.00484.2003.
Lewicki MS. Bayesian modeling and classification of neural signals. *Neural Comput*. 1994:6:1005–1030. https://doi.org/10.1162/neco.1994.6.5.1005.
Lian Y, Almasi A, Grayden DB, Kameneva T, Burkitt AN, Meffin H. Learning receptive field properties of complex cells in V1. *PLoS Comput Biol*. 2021:17:e1007957. https://doi.org/10.1371/journal.pcbi.1007957.
Lin N, Urata S, Cook R, Makishima T. Sex differences in the auditory functions of rodents. *Hear Res*. 2022:419:108271. https://doi.org/10.1016/j.heares.2021.108271.
Linden JF, Schreiner CE. Columnar transformations in auditory cortex? A comparison to visual and somatosensory cortices. *Cereb Cortex*. 2003:13:83–89. https://doi.org/10.1093/cercor/13.1.83.
Liu RC, Schreiner CE. Auditory cortical detection and discrimination correlates with communicative significance. *PLoS Biol*. 2007:5(7):e173. https://doi.org/10.1371/journal.pbio.0050173.

Liu RC, Linden JF, Schreiner CE. Improved cortical entrainment to infant communication calls in mothers compared with virgin mice. *Eur J Neurosci*. 2006:23(11):3087–3097. https://doi.org/10.1111/j.1460-9568.2006.04840.x.

López-Jury L, García-Rosales F, González-Palomares E, Wetekam J, Pasek M, Hechavarria JC. A neuron model with unbalanced synaptic weights explains the asymmetric effects of anaesthesia on the auditory cortex. *PLoS Biol*. 2023:21:e3002013. https://doi.org/10.1371/journal.pbio.3002013.

Lu T, Liang L, Wang X. Neural representations of temporally asymmetric stimuli in the auditory cortex of awake primates. *J Neurophysiol*. 2001:85:2364–2380. https://doi.org/10.1152/jn.2001.85.6.2364.

Mackey CA, Dylla M, Bohlen P, Grigsby J, Hrnicek A, Mayfield J, Ramachandran R. Hierarchical differences in the encoding of sound and choice in the subcortical auditory system. *J Neurophysiol*. 2023:129:591–608. https://doi.org/10.1152/jn.00439.2022.

Malone BJ, Beitel RE, Vollmer M, Heiser MA, Schreiner CE. Spectral context affects temporal processing in awake auditory cortex. *J Neurosci*. 2013:33:9431–9450. https://doi.org/10.1523/JNEUROSCI.3073-12.2013.

Malone BJ, Beitel RE, Vollmer M, Heiser MA, Schreiner CE. Modulation-frequency-specific adaptation in awake auditory cortex. *J Neurosci*. 2015:35:5904–5916. https://doi.org/10.1523/JNEUROSCI.4833-14.2015.

Malone BJ, Heiser MA, Beitel RE, Schreiner CE. Background noise exerts diverse effects on the cortical encoding of foreground sounds. *J Neurophysiol*. 2017:118:1034–1054. https://doi.org/10.1152/jn.00152.2017.

Marmarelis VZ. Modeling methodology for nonlinear physiological systems. *Ann Biomed Eng*. 1997:1997(2):239–251. https://doi.org/10.1152/jn.00152.2017.

Marmarelis VZ, Marmarelis PZ. *Analysis of physiological systems: the white noise approach*. Chacon: Lavoisier; 1978.

Marr D, Hildreth E, E. Theory of edge detection. *Proc R Soc Lond B Biol Sci*. 1980:207:187–217.

Martin LM, García-Rosales F, Beetz MJ, Hechavarría JC. Processing of temporally patterned sounds in the auditory cortex of Seba's short-tailed bat. *Eur J Neurosci*. 2017:46:2365–2379. https://doi.org/10.1111/ejn.13702.

McDermott JH, Simoncelli EP. Sound texture perception via statistics of the auditory periphery: evidence from sound synthesis. *Neuron*. 2011:7:926–940. https://doi.org/10.1016/j.neuron.2011.06.032.

Mechler F, Ringach DL. On the classification of simple and complex cells. *Vis Res*. 2002:42:1017–1033. https://doi.org/10.1016/S0042-6989(02)00025-1.

Mechler F, Victor JD, Purpura KP, Shapley RM. Robust temporal coding of contrast by V1 neurons for transient but not for steady-state stimuli. *J Neurosci*. 1998:18:6583–6598. https://doi.org/10.1523/JNEUROSCI.18-16-06583.1998.

Merzenich MM, Schreiner CE. (1992) mammalian auditory cortex—Some comparative observations. In: Webster DB, Popper AN, Fay RR, editors. *The evolutionary biology of hearing*. New York: Springer; 1992, pp. 673–689.

Meyer AF, Williamson RS, Linden LF, Sahani M. Models of neuronal stimulus-response functions: elaboration, estimation, evaluation. *Front Syst Neurosci*. 2017:10:109. https://doi.org/10.3389/fnsys.2016.00109.

Miller LM, Escabí MA, Read HL, Schreiner CE. Functional convergence of response properties in the auditory thalamocortical system. *Neuron*. 2001:32:151–160. https://doi.org/10.1016/S0896-6273(01)00445-7.

Miller LM, Escabí MA, Read HL, Schreiner CE. Spectro-temporal receptive fields in the lemniscal auditory thalamus and cortex. *J Neurophysiol*. 2002:87:516–527. https://doi.org/10.1152/jn.00395.2001.

Miller OH, Moran JT, Hall BJ. Two cellular hypotheses explaining the initiation of ketamine's antidepressant actions: direct inhibition and disinhibition. *Neuropharmacology*. 2016:100:17–26. https://doi.org/10.1016/j.neuropharm.2015.07.028.

Movshon JA, Thompson ID, Tolhurst DJ. Receptive field organization of complex cells in the cat's striate cortex. *J Physiol*. 1978:283:79–99. https://doi.org/10.1113/jphysiol.1978.sp012489.

Nelken I, Calford MB. Processing strategies in auditory cortex: Comparison with other sensory modalities. In: Winer JA, Schreiner CE, editors. *The auditory cortex*. New York, Springer; 2011. p. 643–656, 10.1007/978-1-4419-0074-6_30.

Niell CM, Stryker MP. Highly selective receptive fields in mouse visual cortex. *J Neurosci*. 2008:28:7520–7536. https://doi.org/10.1523/JNEUROSCI.0623-08.2008.

Nourski KV, Steinschneider M, Rhone AE, Krause BM, Mueller RN, Kawasaki H, Banks MI. Cortical responses to vowel sequences in awake and anesthetized states: a human intracranial electrophysiology study. *Cereb Cortex*. 2021:31:5435–5448. https://doi.org/10.1093/cercor/bhab168.

Ohzawa I, DeAngelis GC, Freeman RD. Encoding of binocular disparity by complex cells in the cat's visual cortex. *J Neurophysiol*. 1997:77:2879–2909. https://doi.org/10.1152/jn.1997.77.6.2879.

Olsen T, Hasenstaub A. Offset responses in the auditory cortex show unique history dependence. *J Neurosci*. 2022:42:7370–7385. https://doi.org/10.1523/JNEUROSCI.0494-22.2022.

Pollen DA, Ronner SF. Spatial computation performed by simple and complex cells in the visual cortex of the cat. *Vis Res*. 1982:22(1):101–118. https://doi.org/10.1016/0042-6989(82)90172-9.

Pollen DA, Gaska JP, Jacobson lD. Responses of simple and complex cells to compound sine-wave gratings. *Vis Res*. 1988:28(1):25–39. https://doi.org/10.1016/S0042-6989(88)80003-8.

Pramodsingh HT, Fitzgerald PJ, Hsiao SS. Second-order receptive fields reveal multidigit interactions in area 3b of the macaque monkey. *J Neurophysiol*. 2012:108:243–262. https://doi.org/10.1152/jn.01022.2010.

Priebe NJ, Mechler F, Carandini M, Ferster D. The contribution of spike threshold to the dichotomy of cortical simple and complex cells. *Nat Neurosci*. 2004:7:1113–1122. https://doi.org/10.1038/nn1310.

Qiu A, Schreiner CE, Escabi MA. Gabor analysis of auditory midbrain receptive fields: spectro-temporal and binaural composition. *J Neurophysiol*. 2003:90:456–476. https://doi.org/10.1152/jn.00851.2002.

Rajan K, Bialek W. Maximally informative "stimulus energies" in the analysis of neural responses to natural signals. *PLoS One*. 2013:8:e71959. https://doi.org/10.1371/journal.pone.0071959.

Ramamurthy DL, Recanzone GH. Spectral and spatial tuning of onset and offset response functions in auditory cortical fields A1 and CL of rhesus macaques. *J Neurophysiol*. 2017:117:966–986. https://doi.org/10.1152/jn.00534.2016.

Rauschecker JP. Processing of complex sounds in the auditory cortex of cat, monkey, and man. *Acta Otolaryngol Suppl*. 1997:532:34–38.

Rauschecker JP. Auditory and visual cortex of primates: a comparison of two sensory systems. *Eur J Neurosci*. 2015:41:579–585. https://doi.org/10.1111/ejn.12844.

Rust NC, Schwartz O, Movshon JA, Simoncelli EP. Spatiotemporal elements of macaque v1 receptive fields. *Neuron*. 2005:46:945–956. https://doi.org/10.1016/j.neuron.2005.05.021.

Sadagopan S, Wang X. Nonlinear spectro-temporal interactions underlying selectivity for complex sounds in auditory cortex. *J Neurosci*. 2009:29:11192–11202. https://doi.org/10.1523/JNEUROSCI.1286-09.2009.

Sakai K, Tanaka S. Spatial pooling in the second-order spatial structure of cortical complex cells. *Vis Res*. 2000:40:855–871. https://doi.org/10.1016/S0042-6989(99)00230-8.

Schaefer MK, Kössl M, Hechavarría JC. Laminar differences in response to simple and spectro-temporally complex sounds in the primary auditory cortex of ketamine-anesthetized gerbils. *PLoS One*. 2017:12:e0182514. https://doi.org/10.1371/journal.pone.0182514.

Schiff ML, Reyes AD. Characterization of thalamocortical responses of regular-spiking and fast-spiking neurons of the mouse auditory cortex in vitro and in silico. *J Neurophysiol*. 2012:107:1476–1488. https://doi.org/10.1152/jn.00208.2011.

See JZ, Homma NY, Atencio CA, Sohal VS, Schreiner CE. Information diversity in individual auditory cortical neurons is associated with functionally distinct coordinated neuronal ensembles. *Sci Rep*. 2021:11(1):4064. https://doi.org/10.1038/s41598-021-83565-7.

Shams L, von der Malsburg C. The role of complex cells in object recognition. *Vis Res*. 2002:42:2547–2554. https://doi.org/10.1016/S0042-6989(02)00202-X.

Sharpee T. Computational identification of receptive fields. *Annu Rev Neurosci*. 2013:36:103–120. https://doi.org/10.1146/annurev-neuro-062012-170253.

Sharpee T. Toward functional classification of neuronal types. *Neuron*. 2014:83:1329–1334. https://doi.org/10.1016/j.neuron.2014.08.040.

Sharpee T. How invariant feature selectivity is achieved in cortex. *Front Synaptic Neurosci*. 2016:8:26.

Sharpee T, Rust NC, Bialek W. Analyzing neural responses to natural signals: maximally informative dimensions. *Neural Comput*. 2004:16:223–250. https://doi.org/10.1162/089976604322742010.

Sharpee T, Sugihara H, Kurgansky AV, Rebrik SP, Stryker MP, Miller KD. Adaptive filtering enhances information transmission in visual cortex. *Nature*. 2006:439:936–942. https://doi.org/10.1038/nature04519.

Sharpee T, Miller KD, Stryker MP. On the importance of static nonlinearity in estimating spatiotemporal neural filters with natural stimuli. *J Neurophysiol*. 2018:99:2496–2509. https://doi.org/10.1152/jn.01397.2007.

Shih JY, Yuan K, Atencio CA, Schreiner CE. Distinct manifestations of cooperative, multidimensional stimulus representations in different auditory forebrain stations. *Cereb Cortex*. 2020:30:3130–3147. https://doi.org/10.1093/cercor/bhz299.

Skottun BC, De Valois RL, Grosof DH, Movshon JA, Albrecht DG, Bonds AB. Classifying simple and complex cells on the basis of response modulation. *Vis Res*. 1991:31:1079–1086. https://doi.org/10.1016/0042-6989(91)90033-2.

Suga N, O'Neill W, Kujirai K, Manabe T. Specificity of combination-sensitive neurons for processing of complex biosonar signals in auditory cortex of the mustached bat. *J Neurophysiol*. 1983:49:1573–1626. https://doi.org/10.1152/jn.1983.49.6.1573.

Syka J, Šuta D, Popelář J. Responses to species-specific vocalizations in the auditory cortex of awake and anesthetized Guinea pigs. *Hear Res*. 2005:206:177–184. https://doi.org/10.1016/j.heares.2005.01.013.

Tian B, Kuśmierek P, Rauschecker JP. Analogues of simple and complex cells in rhesus monkey auditory cortex. *Proc Natl Acad Sci USA*. 2013:110(19):7892–7897. https://doi.org/10.1073/pnas.1221062110.

Touryan J, Lau B, Dan Y. Isolation of relevant visual features from random stimuli for cortical complex cells. *J Neurosci*. 2002:22:10811–10818. https://doi.org/10.1523/JNEUROSCI.22-24-10811.2002.

Van den Bergh G, Zhang B, Arckens L, Chino YM. Receptive-field properties of V1 and V2 neurons in mice and macaque monkeys. *J Comp Neurol*. 2010:518:2051–2070. https://doi.org/10.1002/cne.22321.

Van Hooser SD. Similarity and diversity in visual cortex: is there a unifying theory of cortical computation? *Neuroscientist*. 2007:13:639–656. https://doi.org/10.1177/1073858407306597.

Victor JD, Purpura KP. Spatial phase and the temporal structure of the response to gratings in V1. *J Neurophysiol*. 1998:80:554–571. https://doi.org/10.1152/jn.1998.80.2.554.

Vintch B, Movshon JA, Simoncelli EP. A convolutional subunit model for neuronal responses in macaque V1. *J Neurosci*. 2015:35:14829–14841. https://doi.org/10.1523/JNEUROSCI.2815-13.2015.

Walker KMM, Ahmed B, Schnupp JWH. Linking cortical spike pattern codes to auditory perception. *J Cogn Neurosci*. 2008:20:135–152. https://doi.org/10.1162/jocn.2008.20012.

Wang X, Kadia SC. Differential representation of species-specific primate vocalizations in the auditory cortices of marmoset and cat. *J Neurophysiol*. 2001:86:2616–2620. https://doi.org/10.1152/jn.2001.86.5.2616.

Wehr M, Zador AM. Balanced inhibition underlies tuning and sharpens spike timing in auditory cortex. *Nature*. 2003:426:442–446. https://doi.org/10.1038/nature02116.

Williamson RS, Ahrens MB, Linden JF, Sahani M. Input-specific gain modulation by local sensory context shapes cortical and thalamic responses to complex sounds. *Neuron*. 2016:91:467–481. https://doi.org/10.1016/j.neuron.2016.05.041.

Zahorian SA, Jagharghi AJ. Spectral-shape features versus formants as acoustic correlates for vowels. *J Acoust Soc Am*. 1993:94:1966–1982. https://doi.org/10.1121/1.407520.

Zhang Y, Li Z, Dong H, Yu T. Effects of general anesthesia with propofol on thalamocortical sensory processing in rats. *J Pharmacol Sci*. 2014:126:370–381. https://doi.org/10.1254/jphs.14153FP.

Ziemba CM, Perez RK, Pai J, Kelly JG, Hallum LE, Shooner C, Movshon JA. Laminar differences in responses to naturalistic texture in macaque V1 and V2. *J Neurosci*. 2019:39:9748–9756. https://doi.org/10.1523/JNEUROSCI.1743-19.2019.